Journal of Materials Research and Technology 36 (2025) 2977–2993

Contents lists available at ScienceDirect

Journal of Materials Research and Technology

journal homepage: www.elsevier.com/locate/jmrt

# Lightweight design of polymeric thin-walled components: Latticization and elastic–plastic homogenization

L. Romanelli [a,*], C. Santus [a], I. Senegaglia [a], F. Tamburrino [a], M. Controzzi [b], A. Corrado [c], M. Perini [d], D. Kumar [e], R. De Biasi [f,c], M. Benedetti [c]

[a] Department of Civil and Industrial Engineering, University of Pisa, Pisa, Italy
[b] The BioRobotics Institute, Scuola Superiore Sant'Anna, Pisa, Italy
[c] Department of Industrial Engineering, University of Trento, Trento, Italy
[d] ProM Facility of Trentino Sviluppo S.p.A., Rovereto, Italy
[e] Department of Mechanical Engineering, Indian Institute of Technology (BHU), Varanasi, India
[f] Department of Chemical Engineering Materials Environment, Sapienza University, Roma, Italy

ARTICLE INFO

*Keywords:*
Polyamide 12
Multi jet fusion
Lattice structures
Homogenization
Periodic boundary conditions
Anisotropic plastic behaviour

ABSTRACT

The demand for lightweight yet mechanically robust components has driven the exploration of lattice structures, which offer superior weight-to-strength ratios compared to traditional bulk materials. This study investigates the elastic–plastic behaviour of Polyamide 12 (PA12) lattice structures manufactured via multi jet fusion (MJF). The research combines experimental, numerical, and theoretical approaches to develop a robust framework for the mechanical homogenization of these structures. Tensile tests were performed on bulk and graded lattice specimens to characterize their constitutive behaviour. A simplified homogenization method, integrating periodic boundary conditions (PBCs) with the Hill yielding criterion and Levy-Mises plastic flow rule, was developed to model the anisotropic plastic response of representative volume elements (RVEs). This framework accounts for direction-dependent hardening, enabling efficient prediction of lattice behaviour under complex loading scenarios. Numerical simulations of homogenized RVEs reflected experimental results with a good level of accuracy, validating the model's ability to capture both elastic and plastic deformation regimes. Findings highlight the potential of the proposed methodology for structural optimization and mechanical performance prediction in applications requiring lightweight and durable materials, such as automotive, aerospace, and biomedical devices.

## 1. Introduction

In recent years, additive manufacturing (AM) has revolutionized the way industries approach the design and production of complex mechanical components. One of the most compelling advantages of AM lies in its ability to create intricate geometries, such as lattice structures [1,2], that provide significant weight reduction while maintaining high mechanical performances. Lattice structures are increasingly used in applications where weight savings and material efficiency are critical, such as in aerospace [3–7] automotive [8,9], and medical devices [10–13]. However, the challenge of material selection remains a key factor in determining the viability of these structures in industrial settings. While metallic materials produced through techniques such as laser powder bed fusion (LPBF) offer excellent mechanical properties [14–16], they come with certain drawbacks - chief among them being the high manufacturing cost. Metals, though suitable for high-performance applications, tend to be expensive to process considering the corresponding additive manufacturing process, which is for example laser powder bed fusion. This results in very high costs when low-volume production runs or complex geometries like lattice structures are manufactured. In this scenario, polymeric materials, particularly thermoplastics, emerge as a cost-effective alternative [17]. Materials such as PA are widely used in industrial relevant AM applications and PA12 stands out as one of the most popular materials, exhibiting a strong balance between mechanical strength and flexibility, and it also has the possibility, as other polymeric materials, to enhance its durability thanks to surface treatments [18–20]. In addition to its inherent material properties, PA12 is also highly compatible with high productivity and high-quality AM technologies, such as selective laser sintering (SLS) and MJF [8]. MJF technology, developed by HP, is an additive manufacturing process where a thin layer of polymer powder is spread on a build platform. A fusing agent is selectively applied, and

* Corresponding author.
*E-mail address:* lorenzo.romanelli@phd.unipi.it (L. Romanelli).

https://doi.org/10.1016/j.jmrt.2025.03.137
Received 6 February 2025; Accepted 15 March 2025
Available online 25 March 2025

**Nomenclature**

| | |
|---|---|
| PA | Polyamide |
| MJF | Multi jet fusion |
| RVE | Representative volume element |
| AM | Additive manufacturing |
| LPBF | Laser powder bed fusion |
| SLS | Selective laser sintering |
| B specimen | Bulk specimen |
| FE | Finite element |
| BCC | Body centred cubic |
| PBCs | Periodic boundary conditions |
| AR | Aspect ratio |
| $E_{yy}$ | Young modulus of the homogenized model along $y$ direction |
| $E_{xx}$ | Young modulus of the homogenized model along $x$ direction |
| $G_{xy}$ | Shear modulus of the homogenized model in the $xy$ plane |
| $\nu_{xy}$ | Poisson ratio of the homogenized model indicating the strain in $y$ direction after a uniaxial loading in $x$ direction |
| $\nu_{yx}$ | Poisson ratio of the homogenized model indicating the strain in $x$ direction after a uniaxial loading in $y$ direction |
| $F_x$, $F_y$ | Forces in $x$ and $y$ directions |
| $a_1$, $a_2$, $t$ | Height, width and thickness of the homogenized model |
| $\sigma_{yy}$, $\sigma_{xx}$, $\tau_{xy}$ | Components of the planar Cauchy tensor |
| $\varepsilon_{yy}$, $\varepsilon_{xx}$, $\gamma_{xy}$ | Components of the planar strains matrix |
| $\varepsilon^{el}_{yy}$, $\varepsilon^{el}_{xx}$, $\gamma^{el}_{xy}$ | Components of the planar elastic strains matrix |
| $u_x$, $u_y$ | Imposed displacements along $x$ and $y$ directions |
| $d_x$ | Displacement along $x$ direction due to uniaxial loading along $y$ direction |
| $d_y$ | Displacement along $y$ direction due to uniaxial loading along $x$ direction |
| $\varepsilon^{pl}_{yy}$, $\varepsilon^{pl}_{xx}$, $\gamma^{pl}_{xy}$ | Components of the planar plastic strains matrix |
| $d\varepsilon^{pl}_{yy}$, $d\varepsilon^{pl}_{xx}$, $d\gamma^{pl}_{xy}$ | Components of the incremental planar plastic strain matrix |
| $R_{xx}$, $R_{yy}$, $R_{xy}$ | Hill stress ratios |
| $k$ | Biaxiality ratio |
| $F$, $G$, $H$, $N$ | Hill yielding criterion constants |
| $\sigma_{eq}$ | Equivalent stress according to Hill yielding criterion |
| $\varepsilon^{pl}_{eq}$ | Equivalent plastic strain according to Hill yielding criterion |
| $d\lambda$ | Constants to calculate the incremental plastic strains values |
| $\sigma_{0,xx}$ | First yielding point due to uniaxial loading in $x$ direction |
| $\sigma_{0,yy}$ | First yielding point due to uniaxial loading in $y$ direction |
| $\tau_{0,xy}$ | First yielding point due to shear loading in $xy$ plane |
| $d$, $\theta$ | Strut diameter and strut helix angle |
| $T$ specimen | Triangular specimen |
| S specimen | Shell specimen |
| $D_1$, $D_2$ | Ellipse semi-axes of the real cross-section of the bulk specimens |
| $Area$ | Area of the real cross-section of the bulk specimens |
| $\sigma$ | Longitudinal stress obtained from tensile tests |
| $\varepsilon$ | Longitudinal strain obtained from tensile tests |
| $u$ | Longitudinal displacement obtained from tensile tests |
| $F$ | Longitudinal force obtained from tensile tests |
| $E$ | Young modulus of bulk specimens |
| $\nu$ | Poisson's ratio of bulk specimens |
| $G$ | Shear modulus of bulk specimens |
| $\varepsilon^{pl}$ | Plastic strain obtained from tensile tests on bulk specimens |
| $R_{ext}$ | External radius of the homogenized model of the first layer of lattice specimen |
| $R_{int}$ | Internal radius of the homogenized model of the first layer of lattice specimen |
| $M_y$ | Axial moment obtained from FE simulations of 1/40 of the central layers of $T$ and S specimens |
| $\tau_{\theta y}$ | Shear stress in a cylindrical coordinate system |
| $\gamma_{\theta y}$ | Shear strain in a cylindrical coordinate system |
| $L_0$ | Initial gauge length of the extensometer |
| $\Delta u_y$ | Relative displacement of the extremities of the extensometer |

infrared energy sinters the material layer-by-layer, forming the desired components. Interestingly, the mechanical properties of this material can be enhanced thanks to the insertion in the polymeric matrix of heterogeneous elements such as glass beads [21] or polyamide [22].

Different authors analysed the mechanical properties of PA12 – MJF, identifying the differences between this specific method and SLS manufacturing technique [8,18,23–27]. The material properties are found to be dependent not only on the printing direction of the components, but also on the component position in the printing chamber [19,25,28]. As presented by Chen et al. [28], the different thermal history of components printed in the centre of the printing volume or on the edges are linked to different crystallization and therefore to different mechanical properties. Nevertheless, this manufacturing process was deeply analysed and identified equivalent or outperforming SLS components in terms of surface quality and materials properties repeatability, and PA12 – MJF was recognized suitable for industrial usage [8].

To fully capitalize on the potential of PA12 – MJF lattice structures, it is crucial to develop accurate predictive models that can simulate their mechanical behaviour. These models need to take into account two different challenges: firstly, the nonlinear behaviour of the bulk PA12 – MJF material has to be characterized and lastly, the specific mechanical properties of the designed lattice structures have to be estimated. Different authors studied the mechanical properties of PA12 – MJF bulk specimens (B specimens) and characterized the nonlinear stress–strain relation of this polymeric material [29–33]. Several authors agree in describing the stress–strain curve with an initial linear part followed by a progressive loss of linearity with no clear yielding point. To describe this behaviour, Bian et al. [34] developed an

isotropic hardening rule, while Avanzini et al. [17] used the Ramberg–Osgood model. Lattice structures, due to their inherent geometrical complexity and non-homogeneous nature, exhibit specific mechanical responses and pose a challenge in both design and simulation given that the traditional modelling techniques often fall short in efficiently predicting the behaviour of such structures under quasi-static loads. Solid finite element (FE) modelling is indeed the first answer for estimating the mechanical behaviour of complex structures. However, this technique is highly computational demanding and may not be appropriate for design or optimization needs. For these reasons, researchers focused their attention on computational efficient models able to fully capture not only the linear behaviour but also the nonlinear response of these structures. Among these, the homogenization technique has reached high interest in the last years. Homogenization technique is underpinned by the idea of modelling complex lattice structures by approximating them as homogeneous materials with equivalent mechanical properties [35–38]. A RVE – a limited lattice sub-volume that typifies the overall material behaviour – can be used to efficiently predict the mechanical response of the entire lattice structure [39–44], and applications of homogenization enable the design of lightweight lattice components, providing significant computational efficiency [45–48]. Given that the output of the homogenization can be used in structural design of components that operate beyond the elastic limit, such as in impact tests [49–54], the plastic characterization of lattice structures is a crucial aspect to be investigated. Different approaches were proposed in the literature to describe the plastic behaviour of lattice structures, Gümrük et al. [55] experimentally characterized the plastic collapse envelope of body centred cubic (BCC) lattice units with tensile, shear and compression tests, while in [56–60] the struts were modelled with beams, and analytical analyses were implemented to characterize the first yielding points of RVEs considering tensile and shear loadings in the various directions. The analytical results were then validated with FE simulations and or mechanical tests. In addition to this, characterizing the entire plastic curve, thus the hardening behaviour, of lattice structures is a challenging task, given that, not only the yielding point, but also the hardening may change in the various directions. Somlo et al. [61] characterized the plastic constitutive law of B specimens with the Hill yielding criterion [62], and then they used it in 3D FE simulations of various RVEs with PBCs. Similarly, Pelegatti et al. [63] characterized the cyclic plastic behaviour of B specimens with Chaboche kinematic hardening model [64–67], then they used it in cyclic plastic 3D FE simulations of RVEs. Besides the classical hardening rules, some researchers tried to propose novel hardening models to capture the anisotropic plastic behaviour of lattice structures. For example, Bahrami Babamiri et al. [68] reformulated the volumetric hardening law [69] into the modified volumetric hardening model in order to predict the anisotropic plastic behaviour of BCC lattice units.

The structural analysis of unit cells is of fundamental importance given that, as shown in Fig. 1(a), certain components contain thin-walled regions where weight can be significantly reduced by introducing a lattice structure. This approach is widely applied in various fields, including prosthetics, ergonomic components, robotic arms, automotive and aerospace engineering, and even large-scale civil structures. In principle, FE analysis can model an entire lattice structure by accurately reproducing its geometric details. However, this method becomes computationally expensive and impractical, particularly for intricate lattice patterns and complex overall geometries. To address this challenge, the lattice structure can be initially approximated as a plain surface, which then requires the use of a homogenization technique to model an equivalent material. As illustrated in Fig. 1(b), the process typically starts from the definition of the overall geometry and applied loads. A specific lattice pattern is then introduced and subsequently replaced by its homogenized material representation. The equivalent material properties are determined by analysing a single RVE through detailed FE simulations. Existing studies primarily focus on elastic homogenization, generating materials with varying levels of anisotropy depending

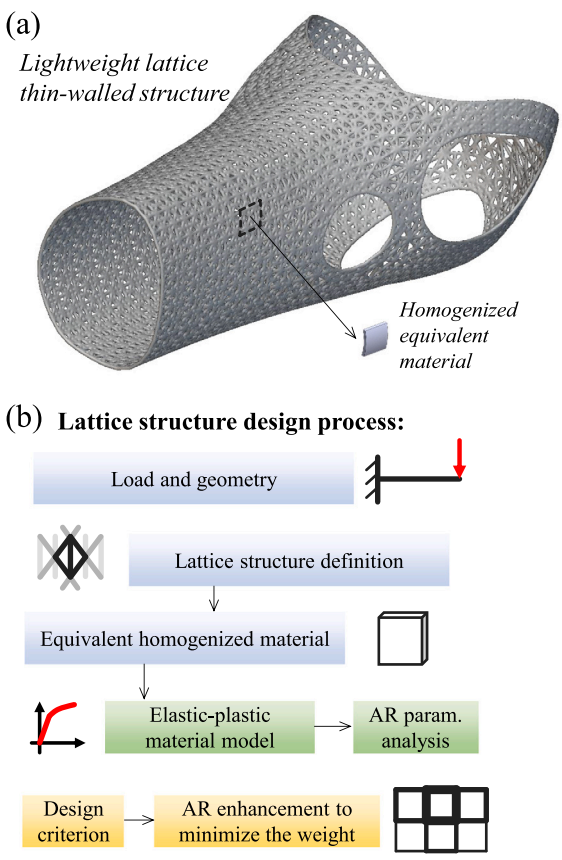


**Fig. 1.** (a) Lightweight lattice thin-walled structure and (b) lattice structure design process.

on the lattice pattern. In contrast, this study extends the approach to include elastic–plastic homogenization. This extension is justified by the assumption that the material must withstand occasional overloads beyond its elastic limit, particularly under accidental or temporary loading conditions. To achieve this, we propose a simplified method to model the different hardening behaviour of RVEs along various directions. For optimization-or at least weight reduction-it is crucial to define the homogenized material properties over a broad range of aspect ratios (AR), where AR is defined as the ratio between the unit cell size and the strut diameter. Once these parametric material properties are established, the lattice structure's local density can be optimized based on stress distribution, ultimately leading to an optimized lattice layout. A key aspect of this procedure is the accurate determination of material properties. This paper presents a comprehensive homogenized model for two different planar lattice patterns fabricated using MJF in PA12, extending the material model to capture a relevant portion of its nonlinear behaviour. The numerical model is then validated through experimental testing on lattice specimens, confirming the ability of the homogenized material model to accurately represent lattice structures.

## 2. Material modelling

In this section the material modelling through Hill yielding criterion and elastic–plastic homogenization is described.

### 2.1. Hill yielding criterion

The compliance elastic matrix for an orthotropic material under a planar loading case can be described by Eq. (1), where $\sigma_{xx}$, $\sigma_{yy}$ and $\tau_{xy}$ are the stress components, $\varepsilon_{xx}^{el}$, $\varepsilon_{yy}^{el}$ and $\gamma_{xy}^{el}$ are the elastic

strain components and $E_{xx}$, $E_{yy}$ are the Young moduli along $x$ and $y$ directions, respectively, while $G_{xy}$ is the shear modulus in $xy$ plane.

$$\begin{pmatrix}\varepsilon_{xx}^{el}\\ \varepsilon_{yy}^{el}\\ \gamma_{xy}^{el}\end{pmatrix}=\begin{pmatrix}\frac{1}{E_{xx}} & & \text{Sym.}\\ -\frac{\nu_{xy}}{E_{xx}} & \frac{1}{E_{yy}} & \\ 0 & 0 & \frac{1}{G_{xy}}\end{pmatrix}\begin{pmatrix}\sigma_{xx}\\ \sigma_{yy}\\ \tau_{xy}\end{pmatrix} \tag{1}$$

The plastic components of the strains can be calculated as $\varepsilon_{xx}^{pl}=\varepsilon_{xx}-\sigma_{xx}/E_{xx}$, $\varepsilon_{yy}^{pl}=\varepsilon_{yy}-\sigma_{yy}/E_{yy}$ and $\gamma_{xy}^{pl}=\gamma_{xy}-\tau_{xy}/G_{xy}$. The equivalent stress $\sigma_{eq}$ and the incremental equivalent plastic strain $d\varepsilon_{eq}^{pl}$ for a planar loading case according to Hill yielding criterion [62] are presented in Eqs. (2) and (3) where $F, G, H$ and $N$ are the Hill constants to be tuned. The Hill stress ratios for the various directions, i.e. $R_{xx}$ for $x$ direction, $R_{yy}$ for $y$ direction and $R_{xy}$ for shear loading in $xy$ plane are presented in Eq. (4), and they are defined as the ratio between the stresses in the various directions ($\sigma_{xx}$, $\sigma_{yy}$ and $\tau_{xy}$) and the reference stress $\sigma_0$. The plastic flow rule proposed by Levy-Mises is presented in Eqs. (5), and it is important to remark that this latter is energetically associated with Hill yielding criterion, thus it provides the satisfaction of the thermodynamics boundaries imposed by plastic strains. The plastic flow rule does not enable the computation of the incremental plastic strains, while it only helps to understand which components of the plastic strain tensor are not null. This latter aspect is motivated by the fact that the constant $d\lambda$ is unknown in Eq. (5), and the introduction of a hardening rule is necessary to calculate it. Considering the reference stress as $\sigma_{yy}$, i.e. $\sigma_0=\sigma_{yy}$, equations from (2) to (5) enables to analyse different loading cases in the various directions. The equivalent stress is equal to $\sigma_{eq}=\sigma_{yy}$ for the uniaxial loading along $y$ direction, and this is expected if the plastic curve along $y$ direction is defined as the reference curve, while it is equal to $\sigma_{eq}=\sigma_{xx}\sqrt{G+H}$ for the uniaxial loading along $x$ direction and to $\sigma_{eq}=\tau_{xy}\sqrt{2N}$ for the shear loading in $xy$ plane. As concerns the strain, the incremental equivalent plastic strain is equal to $d\varepsilon_{eq}^{pl}=d\varepsilon_{yy}^{pl}$ for the uniaxial loading along $y$ direction, while it is equal to $d\varepsilon_{eq}^{pl}=d\varepsilon_{xx}^{pl}/\sqrt{G+H}$ for the uniaxial loading along $x$ direction and to $d\varepsilon_{eq}^{pl}=d\gamma_{xy}^{pl}/\sqrt{2N}$ for the shear loading in $xy$ plane. Once the yielding criterion and the plastic flow rule are presented, the hardening model has to be introduced to completely define the plastic behaviour. The description of the hardening of an orthotropic material is a challenging task, and it generally requires the introduction of complex material models. In order to achieve a simplified numerical modelling that can be implemented with the available techniques of commercial FE software, a workflow is here proposed. The hardening rule is introduced in the FE software with a lookup table representing the plastic curve of RVE along one direction. If, for example, $y$ direction is chosen, the quantities $\sigma_{yy}$ and $\varepsilon_{yy}^{pl}$ have to be introduced in FE. Given that the hardening of RVE in the other directions ($x$ direction and $xy$ plane) are different with respect to that in $y$ direction, they are defined by finding the appropriate parameters $R_{xx}$ and $R_{xy}$ that scale the plastic curves along $x$ direction and in $xy$ plane to fit the plastic curve along $y$ direction. To perform this scaling operation, the plastic curves have to be compared in an appropriate plane where the equivalent plastic strain and the equivalent stress are reported on $x$ and $y$ axes, respectively. Regarding the shear loading cases, the quantities $\varepsilon_{yy}^{pl}$ and $\gamma_{xy}^{pl}R_{xy}/\sqrt{3}$ are reported on $x$ axis, while $\sigma_{yy}$ and $\sqrt{3}\tau_{xy}/R_{xy}$ are the quantities on $y$ axis. The objective of the proposed algorithm is to obtain the coefficient $R_{xy}$ to scale the quantity $\sqrt{3}\tau_{xy}$ to fit the master curve $\sigma_{yy}$. It is important to remark that during the fitting operation both the quantities $\sqrt{3}\tau_{xy}/R_{xy}$ and $\gamma_{xy}^{pl}R_{xy}/\sqrt{3}$ have to be contemporary updated given their dependence on $R_{xy}$. The same reasoning can be made for the loading case along $x$ direction. In this case the quantities $\varepsilon_{yy}^{pl}$ and $R_{xx}\varepsilon_{xx}^{pl}$ are reported on $x$ axis, while $\sigma_{yy}$ and $\sigma_{xx}/R_{xx}$ are the quantities on $y$ axis, and the quantities $\sigma_{xx}/R_{xx}$ and $R_{xx}\varepsilon_{xx}^{pl}$ have to be updated during the fitting operation. Hill stress ratios $R_{xy}$ and $R_{xx}$ can be obtained with a pointwise fitting operation with the least squares method. However, the determination of $R_{xx}$ and $R_{xy}$ is not enough to obtain the constants $F$, $G$ and $H$ as shown in Eq. (6). For this reason, a biaxial loading case, with $\sigma_{yy}=k\sigma_{xx}$ and $\tau_{xy}=0$ can be used to tune the value of constant $H$. In this latter condition, the equivalent stress and the equivalent plastic strain are equal to $\sigma_{eq}=\sigma_{xx}\sqrt{\left(1/R_{xx}^2\right)+k^2-2kH}$ and $\varepsilon_{eq}^{pl}=\varepsilon_{xx}^{pl}\frac{\sqrt{\left(1/R_{xx}^2\right)+k^2-2kH}}{\left(\left(1/R_{xx}^2\right)-kH\right)}$, respectively. The objective is to identify the value of $H$ that scales the equivalent quantities obtained from the biaxial loading condition to the reference stress and plastic strain along $y$ direction, and this fitting operation does not depend on the biaxiality ratio $k$. Once the value of $H$ is obtained, the values of the constants $F$ and $G$ can be updated according to Eq. (6).

$$\sigma_{eq}=\sqrt{(G+H)\sigma_{xx}^2+(F+H)\sigma_{yy}^2-2H\sigma_{xx}\sigma_{yy}+2N\tau_{xy}^2} \tag{2}$$

$$d\varepsilon_{eq}^{pl}=\sqrt{\frac{[(F+H)(d\varepsilon_{xx}^{pl})^2+2Hd\varepsilon_{xx}^{pl}d\varepsilon_{yy}^{pl}+(G+H)(d\varepsilon_{yy}^{pl})^2]}{FH+FG+GH}+\frac{2(d\varepsilon_{xy}^{pl})^2}{N}} \tag{3}$$

$$\text{Hill stress ratios:}\begin{cases}R_{xx}=\frac{\sigma_{xx}}{\sigma_0}\\ R_{yy}=\frac{\sigma_{yy}}{\sigma_0}\\ R_{xy}=\frac{\sqrt{3}\tau_{xy}}{\sigma_0}\end{cases} \tag{4}$$

$$\begin{pmatrix}d\varepsilon_{xx}^{pl}\\ d\varepsilon_{yy}^{pl}\\ d\gamma_{xy}^{pl}\end{pmatrix}=\frac{d\lambda}{\sigma_{eq}}\begin{pmatrix}G+H & & \text{Sym.}\\ -H & F+H & \\ 0 & 0 & 2N\end{pmatrix}\begin{pmatrix}\sigma_{xx}\\ \sigma_{yy}\\ \tau_{xy}\end{pmatrix} \tag{5}$$

$$F,G,H,N=\begin{cases}H\text{ obtained from biaxial loading case}\\ F=1-H\\ G=\frac{1}{R_{xx}^2}-H\\ N=\frac{3}{2R_{xy}^2}=\frac{\sigma_{yy}^2}{2\tau_{xy}^2}\end{cases} \tag{6}$$

### 2.2. Homogenization

The reasoning behind the design of lattice specimens used in this research is presented in Fig. 2. It drew an initial inspiration from ASTM D638 to ensure consistency and reliability in mechanical performance evaluation. The base design is a cyclical X shaped strut based lattice as shown in Fig. 2(a). The gauge region, typical of a standard specimen, was designed with constant diameter and helyx angle of the struts, to maintain consistency in tensile properties for controlled and reproducible responses to the applied loads. In the transitional region, the gradual enlargement of the cross-section improved tensile strength and efficiently distributed stress to reduce the likelihood of failure under high strain conditions. By smoothly adjusting the relative angles of the X struts, the impacts on transverse deformation behaviour were controlled, thereby enhancing the structural response based on bending and decreasing transverse stiffness. The transitional regions facilitated gradual geometric changes to prevent abrupt compliance gradients, promoting reliable mechanical evaluation and robust structural behaviour under tensile loading. From that, two distinct design explorations were undertaken, which are shown in Fig. 2(b) and (c).

In the initial experimental setup, the primary cyclic base lattice utilized a configuration consisting of X-I struts, and it was named as triangular specimens (T specimen). The I struts bore the structural loads

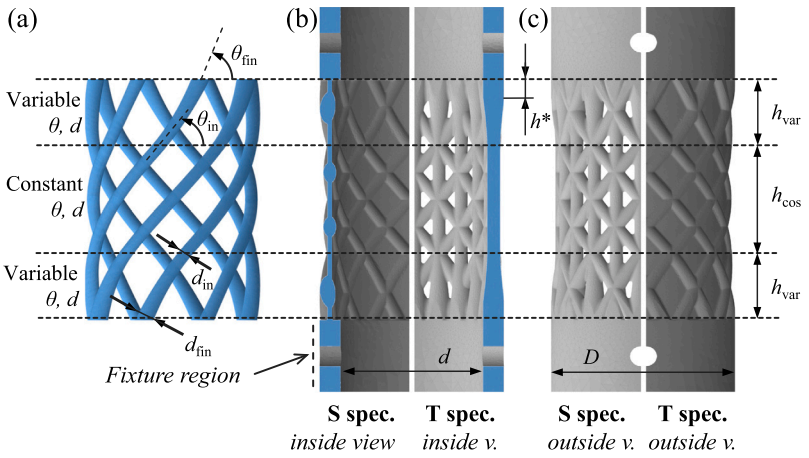


**Fig. 2.** (a) Trend of the quantities $\theta$ (strut angle) and $d$ (strut diameter) along the specimen axis, (b) and (c) design exploration of T and S specimens.

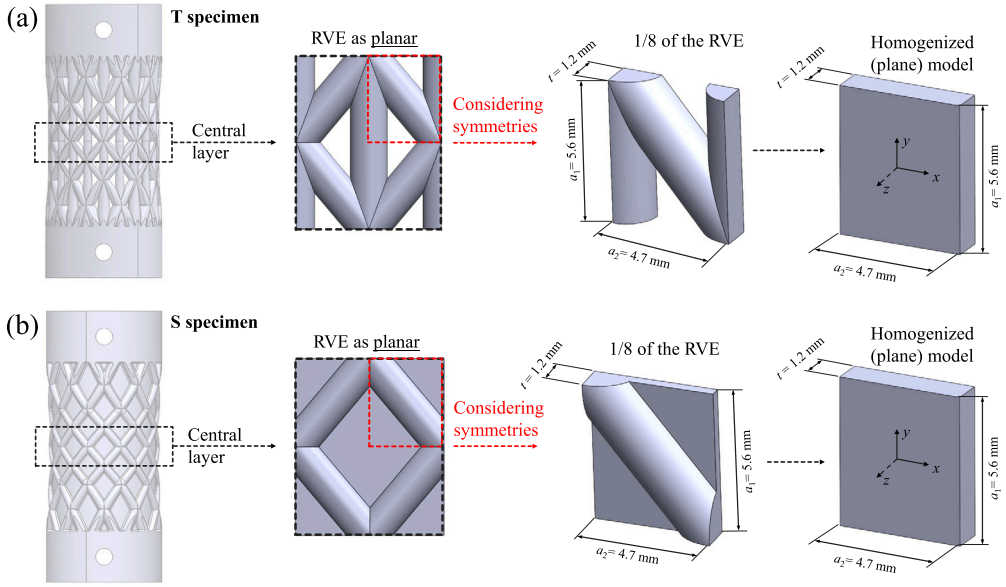


**Fig. 3.** Identification of RVEs of the central layers of (a) T specimen and (b) S specimen.

during tensile testing, while the X struts were tasked with confining transverse deformation, resembling a discretized beam-to-shell effect. On the other hand, in the second design, the X-shaped struts were integrated into a uniform-thickness shell eliminating the vertical struts, and it was named as shell specimen (S specimen). This modification aimed to achieve an evenly distributed shell-effect on the behaviour of the specimen. In the end, the design of T and S specimens was thought with the idea of a possible employment of the lattice specimens in the realization of biomedical tools.

The homogenization of T and S specimens was performed, and, firstly, the RVEs extracted from the central layers of the lattice specimens were homogenized. These layers, according to Fig. 2(a), have constant strut diameters and helix angle. The roundness of the cells was neglected during the homogenization as shown in the centre of Fig. 3 where the RVE, considered planar, is presented, and 1/8 of the RVE was considered thanks to the symmetries as shown in the right part of Fig. 3. The dimensions of the RVEs extracted from the central layers of T and S specimens are shown in Fig. 3, and the aspect ratio (AR) was defined as AR = $a_2/t$ where $a_2$ = 4.7 mm. The AR value of the manufactured and tested lattice units with constant strut diameters and helyx angle was equal to AR = 1.96, and, in order to obtain the dependence of the elastic and plastic quantities of the homogenized models on AR, four other values of AR (AR = 1.47, 2.5, 2.94, 3.5) were considered in the homogenization process. These latter values of AR were not manufactured, but they were only investigated numerically. Before implementing the homogenization process, the level of anisotropy of the RVE was inquired, and, due to the presence of three planes of symmetry, it was modelled as orthotropic according to Neumann principle. In addition to this, considering that the mechanical behaviour of the unit cell along $z$ direction was not meaningful for the structural analysis of this research, the mechanical properties along this direction were neglected during the homogenization. Before analysing the homogenization technique, it is necessary to explain what homogenization means. In the right part of Fig. 3, the unit cells (1/8 because of symmetries) extracted from the central layers of T and S specimens are shown with the corresponding homogenized models. These latter were parallelepipeds that inscribe the RVEs, thus the objective of the homogenization process is to obtain the mechanical properties of equivalent parallelepipeds of the considered RVEs. According to the compliance elastic matrix described in Eq. (1), the quantities to be calculated were $E_{yy}$, $E_{xx}$, $G_{xy}$ and $\nu_{xy}$. The homogenization was also extended to the elastic–plastic field, and the plastic behaviour of the unit cells were obtained in $x$ and $y$ directions for uniaxial loadings, in $xy$ plane for shear loading and the previously described biaxial loading case with $\sigma_{yy} = k\sigma_{xx}$ and $\tau_{xy} = 0$ was also explored.

The homogenization was implemented with FE and with the application of PBCs, which are represented in Fig. 4 for the RVE extracted from the central layer of T specimen. The boundary conditions represented in Fig. 4(a), (b) and (c) correspond to those for uniaxial loading in $y$ direction, for uniaxial loading in $x$ direction and for shear loading in $xy$ plane, respectively. Firstly, the elastic properties of the homogenized model were calculated with linear FE simulations. As concerns the determination of the equivalent Young modulus $E_{yy}$, the boundary conditions are shown in Fig. 4(a), where a nonzero uniform displacement along $y$ direction was imposed on the upper surface and symmetry conditions along $x$, $y$ and $z$ directions were imposed considering that 1/8 of the RVE was considered. The symmetry conditions stand that the displacement is null normally to the faces of symmetry. In addition to this, the planarity was imposed on the face contoured with red dashed lines in Fig. 4(a). Considering that the homogenization technique was thought for infinite periodic units, this latter boundary condition can be motivated by supposing the RVE of Fig. 4 merged in an infinite reticulum of lattice units. If two RVEs are then considered with an imposed displacement on the upper surface along $y$ direction, their common face, which corresponds to that contoured in red in Fig. 4(a), is a face of symmetry thus it must maintain its planarity. After FE simulation, the force $F_y$ on the upper surface was extracted, and the stress $\sigma_{yy}$ was then defined as $\sigma_{yy} = F_y/(a_2\ t)$. Considering $u_y$ as the imposed displacement on the upper surface along $y$ direction, the strain $\varepsilon_{yy}$ was defined as $\varepsilon_{yy} = u_y/a_1$. Finally, the Young modulus $E_{yy}$ of the homogenized model was calculated as $E_{yy} = \sigma_{yy}/\varepsilon_{yy}$. The displacement $d_x$ along $x$ direction was then extracted on the face contoured in red to calculate the Poisson ratio $\nu_{yx}$, which was defined as $\nu_{yx} = (d_x/a_2)/\varepsilon_{yy}$. The displacement $d_x$ was defined positive in case of a contraction of RVE in $x$ direction. The same reasoning was implemented for the determination of $E_{xx}$, shown in Fig. 4(b), where a uniform displacement $u_x$ along $x$ direction was imposed on the face on the right and normal to $x$ axis, and symmetry conditions were applied. In this case, the face contoured in red is the upper face normal to $y$ axis where the planarity was imposed. After FE simulation, the force $F_x$ along $x$ direction was obtained on the same face where the nonzero displacement along $x$ direction was imposed, and the value of $\sigma_{xx}$ was calculated as $\sigma_{xx} = F_x/(a_1\ t)$. The strain $\varepsilon_{xx}$ was defined as $u_x/a_2$, thus the Young modulus $E_{xx}$ of the homogenized model was computed as $E_{xx} = \sigma_{xx}/\varepsilon_{xx}$. Finally, the displacement $d_y$ along $y$ direction was extracted on the face contoured in red, and it was employed to calculate the Poisson ratio $\nu_{xy}$ as $\nu_{xy} = (d_y/a_1)/\varepsilon_{xx}$. Also in this case the displacement $d_y$ was considered positive in case of a contraction of RVE in $y$ direction. After the characterization of the elastic mechanical properties of the homogenized model along $x$ and $y$ directions, it was verified the satisfaction of the relationship $\nu_{xy}/E_{xx} = \nu_{yx}/E_{yy}$, which is described in Eq. (1). Finally, the shear loading condition in $xy$ plane is presented in Fig. 4(c). Also in this case, 1/8 of cell was used in the homogenization process and two of the planes of geometric symmetry were planes of antisymmetry for the loading conditions, while one was a plane of symmetry for the loading conditions. The antisymmetry condition stands that the displacement is null in the plane of antisymmetry. In order to apply a pure shear loading condition, a displacement $u_x$ along $x$ direction was applied on the upper surface of the unit cell, while a displacement along $y$ direction was applied on the right face of the cell, and it was defined as $u_y = u_x(a_2/a_1)$. This latter corresponds, in fact, to the condition of pure shear. After FE simulation, the force $F_x$ along $x$ direction was extracted on the upper surface and the value of the shear stress $\tau_{xy}$ was calculated as $\tau_{xy} = F_x/(a_2\ t)$. In addition to this, the force $F_y$ along $y$ direction was extracted as well on the face where a displacement along $y$ direction was imposed, and the shear stress $\tau_{yx}$ was calculated as $\tau_{yx} = F_y/(a_1\ t)$. Considering the symmetry of the Cauchy stress tensor, it was verified that $\tau_{xy} = \tau_{yx}$. Finally, the shear strain was calculated as $\gamma_{xy} = 2u_x/a_1$ given the small imposed displacements and the shear modulus $G_{xy}$ was obtained as $G_{xy} = \tau_{xy}/\gamma_{xy}$.

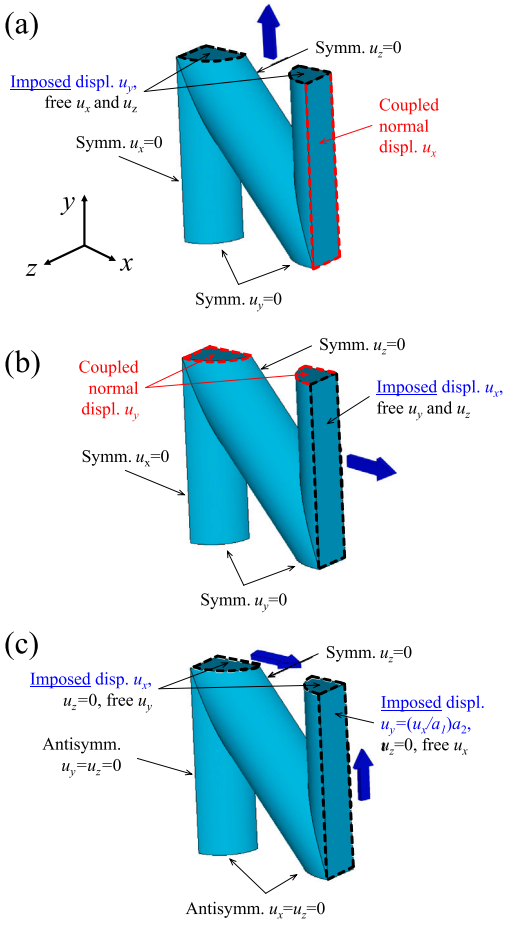


**Fig. 4.** PBCs to perform homogenization of RVE: (a) uniaxial loading along $y$ direction, (b) uniaxial loading along $x$ direction and (c) shear loading in $xy$ plane. (For interpretation of the references to colour in this figure legend, the reader is referred to the web version of this article.)

Once the determination of the elastic mechanical properties of the homogenized model was concluded, the computation of the plastic mechanical properties was implemented. The same boundary conditions of the elastic homogenization described in Fig. 4 were applied, and the plastic homogenization was performed through nonlinear FE simulations. The boundary conditions for the biaxial loading cases, which as described above was fundamental to identify the constant $H$, consisted of merging the constraints of Fig. 4(a) and (b), and in these cases the simulations were stress controlled. The plastic curves along $x$ and $y$ directions, the shear plastic curve in $xy$ plane and the plastic curve of the biaxial loading case were obtained after nonlinear elastic–plastic FE simulations. The mathematical definition of the quantities $\sigma_{yy}$, $\varepsilon_{yy}$, $\sigma_{xx}$, $\varepsilon_{xx}$, $\tau_{xy}$ and $\gamma_{xy}$ after nonlinear FE simulations was equal to that presented above for the determination of the elastic properties, while the plastic components of the strains in the various directions were calculated by subtracting the elastic strain from the total strain. The same PBCs were employed to calculate the elastic and plastic quantities of RVEs with different AR.

The geometries of T and S specimens can be employed in numerical simulations of tensile tests on lattice specimens as shown on the left of Fig. 5(a) and (b). In particular, 1/40 of the entire specimens can be used thanks to symmetries, and, after having applied symmetry constraints and a displacement on the upper surfaces along specimen axes, numerical simulations of tensile tests were implemented. However, this can require high computational cost given the geometry of lattice specimens. The alternative consists in performing numerical simulations of tensile tests on the corresponding homogenized models of T

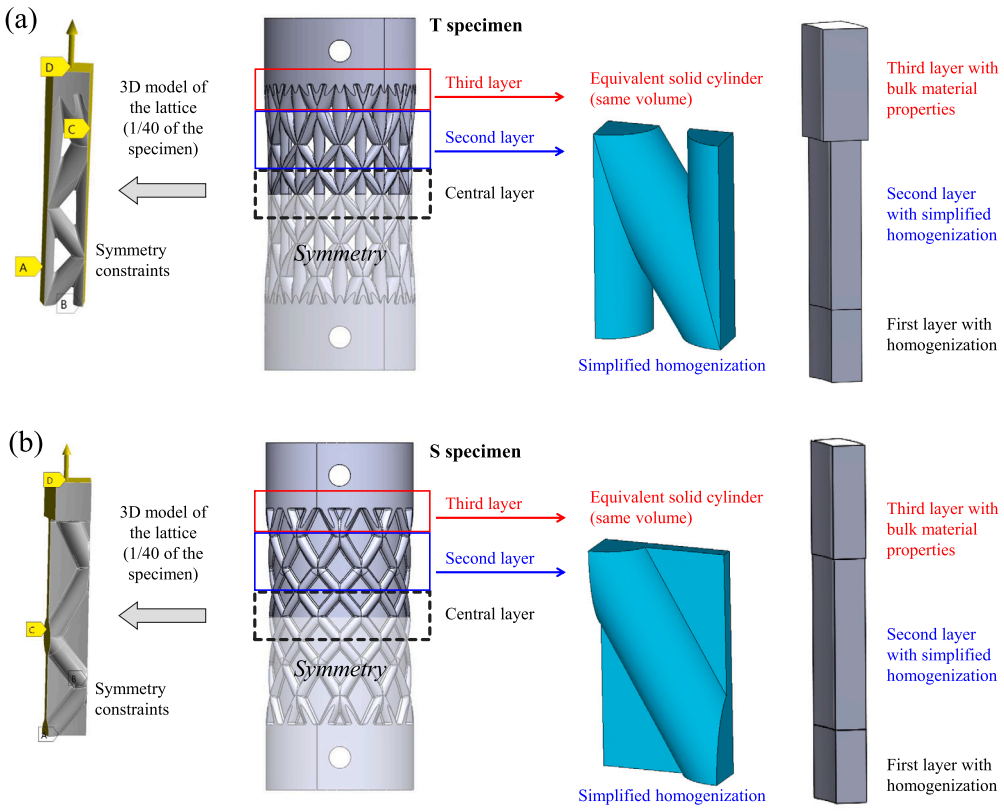


**Fig. 5.** Homogenization of second and third layers of: (a) T specimen and (b) S specimen. (For interpretation of the references to colour in this figure legend, the reader is referred to the web version of this article.)

and S specimens. In fact, the final part of the homogenization process implemented in this research consisted in identifying the mechanical properties of the equivalent homogenized models of T and S specimens. These latter were composed of central layers with constant diameters of the struts $d$ and with constant helix angles $\theta$, and the homogenization of these layers was presented in the previous part of the paper. T and S specimens were also composed of a second layer, contoured with a black dashed line in Fig. 5(a) and (b), and of a third layer, contoured with red dashed line in Fig. 5(a) and (b).

In both specimens, the second layer was composed of lattice units with variable diameters and helyx angles of the struts along specimen axis, while the third layer was composed of lattice units with variable strut diameters and helix angles and of a final bulk hollow cylindrical part where the clamping system was inserted during tensile tests. As shown in Fig. 5(a) and (b), the homogenization of the second layer was performed considering planar RVEs with constant diameters of the struts and helix angles. These latter quantities were obtained as the average of the corresponding quantities at the beginning and at the end of the lattice unit along $y$ direction. The RVEs of the third layers of T and S specimens had a volume density, defined as the ratio between the volume of the RVE and the volume of the circumscribed cylinder, close to 1. For this latter reason, a cylindrical homogenized layer was defined with the same volume of the RVE, and, given the value of the volume density, the constitutive behaviour of the corresponding cylindrical homogenized model was defined as isotropic and equal to that of the bulk material. The simplified RVEs of the second layers of T and S specimens are shown in Fig. 5(a) and (b), where 1/8 of RVEs was considered because of symmetries. The structure of the compliance elastic matrix of these homogenized models had the same structure of that presented in Eq. (1). The boundary conditions used in FE simulations were the same as those presented in Fig. 4. As done for the RVEs with constant strut diameter and helyx angle, firstly linear FE simulations were implemented, and, after, nonlinear FE simulations were performed to characterize the plastic behaviour.

### 2.3. Material characterization

The mechanical drawing of B specimen is reported in Fig. 6(a), and it presents a central zone with uniform diameter where constant values of stress and strain were obtained. The dimension of the diameter was similar to that of the lattice struts, and the central part was linked to the top and bottom zones by fillet radii of 4 mm in order to smooth the stress in the transitional zones. The specimens manufactured and tested in this research were realized with HP jet fusion 4200 3D printing solution using HP 3D high reusability PA 12 material. As well known in literature, the as-built geometry of additive manufactured specimens differs from the as-designed one as highlighted by Raghavendra et al. [70]. To address this issue, a preliminary analysis for retrieving the correct cross section of the specimens has been performed. In accordance with Dallago et al. [71] and the following literature, the cross section of B specimens is not considered circular but as an ellipse as shown in Fig. 6(b), thus cross-sectional area can be computed using Eq. (7), where $D_1$ and $D_2$ are the ellipse semi-axes.

$$Area = \pi \frac{D_1}{2} \frac{D_2}{2} \tag{7}$$

In accordance with Refs. [72–74], $D_1$ and $D_2$ can be measured by using two stereo-optical pictures obtained with a Nikon SMZ25 stereo microscope and elaborated in MATLAB (2024b, MathWorks, USA). An example of the two images is shown in Fig. 6(b), in which the first image was taken on $xy$ plane and the second one was taken on $zy$ plane, where these two planes are orthogonal to each other. Diameters were computed thanks to the algorithm provided by Dallago et al. [71]. The diameters measured from the stereo-optical images are compared to the as-designed dimensions, and the results are reported in Table 1. The mean value of the diameters $D_1$ and $D_2$ are used to compute the mean cross section of each specimen using Eq. (7). From Table 1, it can be observed that the real diameter of B specimens almost

**Table 1**
Measured diameters of PA12 B specimens through the use of stereo-optical images.

| | $D_1$ (mm) | $D_2$ (mm) | Mean area (mm$^2$) |
|---|---|---|---|
| Specimen 1 | 3.1417 ± 0.0026 | 3.1606 ± 0.0027 | 7.7987 |
| Specimen 2 | 3.1496 ± 0.0028 | 3.1795 ± 0.0026 | 7.8651 |
| Theoretical | 3.2 | 3.2 | 8.0425 |
| Error range | From −0.0476 to −0.0609 | From −0.0179 to −0.0421 | From −0.1774 to −0.2438 |

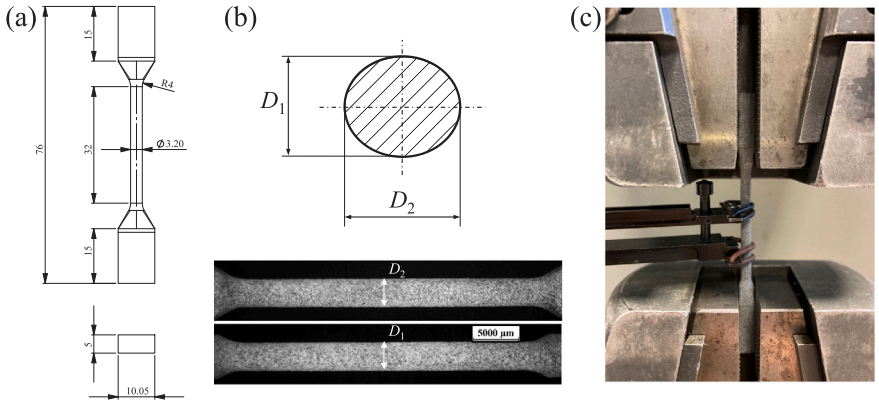


**Fig. 6.** (a) Design of B specimen, (b) schematic representation of the cross-section of as-built B specimens and stereo-optical images in the two orthogonal planes and (c) tensile test on B specimen.

matches the nominal one. The as built diameter is found to be slightly lower, with error ranging between −0.0179 mm to −0.0609 mm. Hence, this reduction in the measured diameters causes a decrease in the measured cross section with an error that lies in between −0.1774 mm$^2$ and −0.2438 mm$^2$. After the completion of the metrological characterization, a quasi-static tensile testing campaign was performed in order to retrieve the mechanical properties of the material. For this purpose, an Instron 5969 equipped with a load cell of 1 kN, an extensometer and self-aligning grips was used. The testing velocity was fixed at 0.1 mm/min and the sampling rate was settled at 2 points per second. An image of the testing set-up is reported in Fig. 6(c).

Quasi-static tensile tests, performed using the above described experimental set-up, were completed and results are shown in Fig. 7 with red and blue curves. Given the low differences between the as-built and as-designed diameters, the longitudinal stress $\sigma$ reported in Fig. 7 was calculated by using the nominal area. In addition, a good repeatability was obtained between the two tested specimens. The possible hyperelastic behaviour of PA12 was also investigated with a loading–unloading test shown in Fig. 7 with the black curve, which highlights that when the stress is reported to a null value, the curve does not go back to the origin of $\sigma$-$\epsilon$ plane, and, in addition, the hysteresis area is not null. These latter findings excluded the possibility of using a hyperelastic model as constitutive law, while the material was modelled considering an initial elastic part and a subsequent elastic–plastic region. The constitutive behaviour obtained from tensile tests on B specimens (blue and red curves of Fig. 7) was used as input to perform FE simulations of lattice units and lattice specimens. The Young modulus of B specimens was obtained with a linear fit in the elastic zone, while the plastic zone was inserted in the FE software through a lookup table. In order to extend the results of FE simulations of RVEs to the maximum value of strain, the red curve of Fig. 7 was used to define the input material properties. The obtained Young modulus was equal to $E = 1119$ MPa, the Poisson ratio was, instead, obtained from the literature for the same material and 3D printing technique, and it was equal to $\nu = 0.4$ according to Avanzini et al. [32]. The constitutive behaviour of bulk PA12 was considered isotropic, thus the shear modulus G was calculated as $G = E/(2(1+\nu))$. The plastic behaviour of the chosen curve is reported in the electronic appendix of the manuscript in terms of plastic strain $\epsilon^{pl}$ and stress $\sigma$.

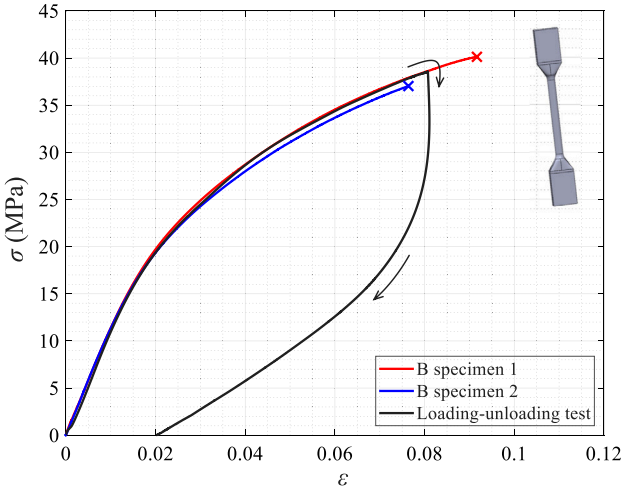


**Fig. 7.** Results of tensile and loading–unloading tests on B specimens. (For interpretation of the references to colour in this figure legend, the reader is referred to the web version of this article.)

### 2.4. Model tuning

The obtained elastic mechanical properties of the homogenized models of the RVEs with $a_1 = 5.6$ mm, $a_2 = 4.7$ mm, constant strut diameters, constant helyx angles and extracted from T and S specimens are presented in Table 2 for the investigated values of AR. The plastic curves along $y$ direction were chosen as reference curves for both T and S specimens to calculate the plastic properties of the homogenized models, and the identified Hill coefficients $F$, $G$, $H$ and $N$ are reported in Table 3 together with the first yielding stresses $\sigma_{0,xx}$, $\sigma_{0,yy}$ and $\tau_{0,xy}$. The results of the elastic–plastic homogenization of RVEs of central layers of T and S specimens with AR = 1.96 are shown in Figs. 8 and 9. In particular, the results of uniaxial loadings along $x$ and $y$ directions are presented in Fig. 8(a), while in Fig. 8(b) the outcomes of the shear loadings in $xy$ plane are shown. In Fig. 9 the results of the scaled plastic curves for uniaxial loading along $x$ direction ((a) and (b)), shear loading in $xy$ plane ((c) and (d)) and biaxial loading ((e) and (f)) are shown,

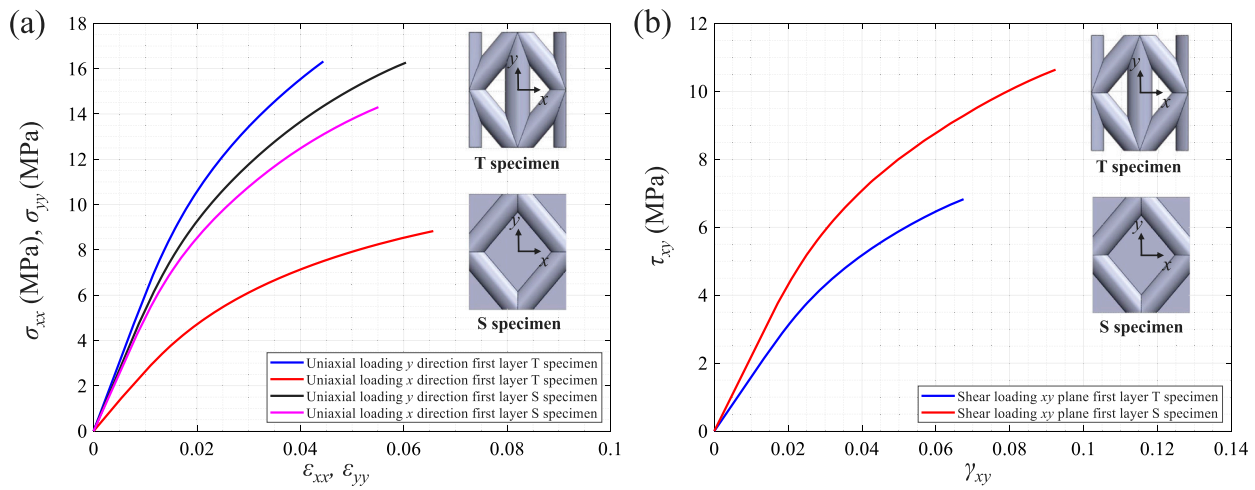


**Fig. 8.** Results of elastic–plastic homogenization of RVEs of the first layers of T and S specimens: (a) uniaxial loadings along $x$ and $y$ directions and (b) shear loadings in $xy$ plane.

and these latter have the aim to fit the reference plastic curves along $y$ direction.

The results of Tables 2 and 3 highlight a marked difference between the Young moduli $E_{xx}$ and $E_{yy}$ and the first yielding stresses $\sigma_{0,xx}$ and $\sigma_{0,yy}$ of the RVE of T specimen, while the same quantities are almost equal for the RVE of S specimen. The shape of the RVE of central layer of T specimen justifies these differences with a higher stiffness along $y$ direction, while the shape of the RVE of the central layer of S specimen justifies the almost equal values of $E_{xx}$ and $E_{yy}$. In fact, if the values of $a_1$ and $a_2$ reported in Fig. 3 had been equal, the values of the Young moduli $E_{xx}$ and $E_{yy}$ and of the first yielding stresses $\sigma_{0,xx}$ and $\sigma_{0,yy}$ would have been identical for the RVE of S specimen. The obtained results of the elastic and plastic quantities of the homogenized models by varying the aspect ratio are also reported in Figs. 10 and 11. Considering the findings of Gibson and Ashby in their pioneering work [75], a power law was employed to describe the dependence of the Young moduli $E_{yy}$ and $E_{xx}$ and of the shear modulus $G_{xy}$, divided by the corresponding bulk quantities $E$ and $G$, on AR. The obtained relationships are presented in Eqs. from (8) to (10). Piecewise linear functions were, instead, employed to represent the dependence of the Poisson ratio and the Hill stress ratios $R_{xx}$ and $R_{xy}$ on AR. The obtained plastic curves along $x$ and $y$ directions and in $xy$ plane for the investigated AR values (AR = 1.47, 1.96, 2.50, 2.94, 3.50) of RVEs of T and S specimens are reported in the electronic appendix of the manuscript.

$$E_{yy}: \begin{cases} \text{T specimen}: E_{yy}/E = 1.16(\text{AR})^{-1.15} \\ \text{S specimen}: E_{yy}/E = 0.607(\text{AR})^{-0.320} \end{cases} \tag{8}$$

$$E_{xx}: \begin{cases} \text{T specimen}: E_{xx}/E = 1.38(\text{AR})^{-2.59} \\ \text{S specimen}: E_{xx}/E = 0.560(\text{AR})^{-0.291} \end{cases} \tag{9}$$

$$G_{xy}: \begin{cases} \text{T specimen}: G_{xy}/G = 0.981(\text{AR})^{-1.28} \\ \text{S specimen}: G_{xy}/G = 0.689(\text{AR})^{-0.332} \end{cases} \tag{10}$$

## 3. Numerical and experimental results

In this section, the numerical and experimental validations of the proposed elastic–plastic homogenization are presented.

**Table 2**
Elastic mechanical properties of the homogenized models of RVEs of T and S specimens by varying AR.

| | $E_{yy}$ (MPa) | $E_{xx}$ (MPa) | $\nu_{xy}$ | $G_{xy}$ (MPa) |
|---|---|---|---|---|
| RVE T specimen (AR = 1.47) | 819 | 588 | 0.279 | 249 |
| RVE T specimen (AR = 1.96) | 609 | 271 | 0.205 | 159 |
| RVE T specimen (AR = 2.50) | 459 | 137 | 0.194 | 118 |
| RVE T specimen (AR = 2.94) | 374 | 91.6 | 0.197 | 97.9 |
| RVE T specimen (AR = 3.50) | 301 | 64.1 | 0.201 | 81.5 |
| RVE S specimen (AR = 1.47) | 609 | 569 | 0.401 | 244 |
| RVE S specimen (AR = 1.96) | 542 | 509 | 0.407 | 219 |
| RVE S specimen (AR = 2.50) | 501 | 477 | 0.409 | 202 |
| RVE S specimen (AR = 2.94) | 480 | 457 | 0.410 | 192 |
| RVE S specimen (AR = 3.50) | 462 | 442 | 0.410 | 183 |

### 3.1. Numerical validations

After the characterization of the elastic–plastic mechanical properties of the homogenized models of RVEs extracted from the central layers of T and S specimens, the obtained results needed to be validate. For this reason, 1/40 of the central layer of both lattice specimens, and corresponding to AR = 1.96, was extracted thanks to the symmetries and it was used for elastic–plastic FE simulations described in Fig. 12 for tensile and shear loadings. In this case the roundness was not neglected, and the corresponding homogenized models consisted of a portion of cylinder that inscribed the simulated lattice units as shown in Fig. 12. The elastic mechanical properties of the homogenized models were defined through the quantities reported in Table 2, while the plastic behaviour was introduced with the plastic curve along $y$ direction ($\sigma_{yy}$ and $\varepsilon_{yy}^{\text{pl}}$) and the Hill ratios obtained with the procedure presented above and shown in Table 3. On the other side, the constitutive behaviour of lattice units in FE simulations was defined through the material properties obtained with tensile tests on B specimens as described in 2.3. The boundary conditions employed in numerical simulations of uniaxial loadings along $y$ direction consisted, for both lattice units and corresponding homogenized models, in the application of a nonzero uniform displacement $u_y$ on the upper surface and in the use of symmetry constraints. Shear elastic–plastic FE simulations were also implemented as shown in Fig. 12, and in this case a nonzero uniform circumferential displacement $u_\theta$ was imposed on the upper surface, while the radial displacement $u_r$ on the same surface was imposed as null. Finally, antisymmetry conditions were applied on the three faces of geometric symmetry. The implemented FE simulations to validate the correctness of elastic–plastic shear properties of the homogenized

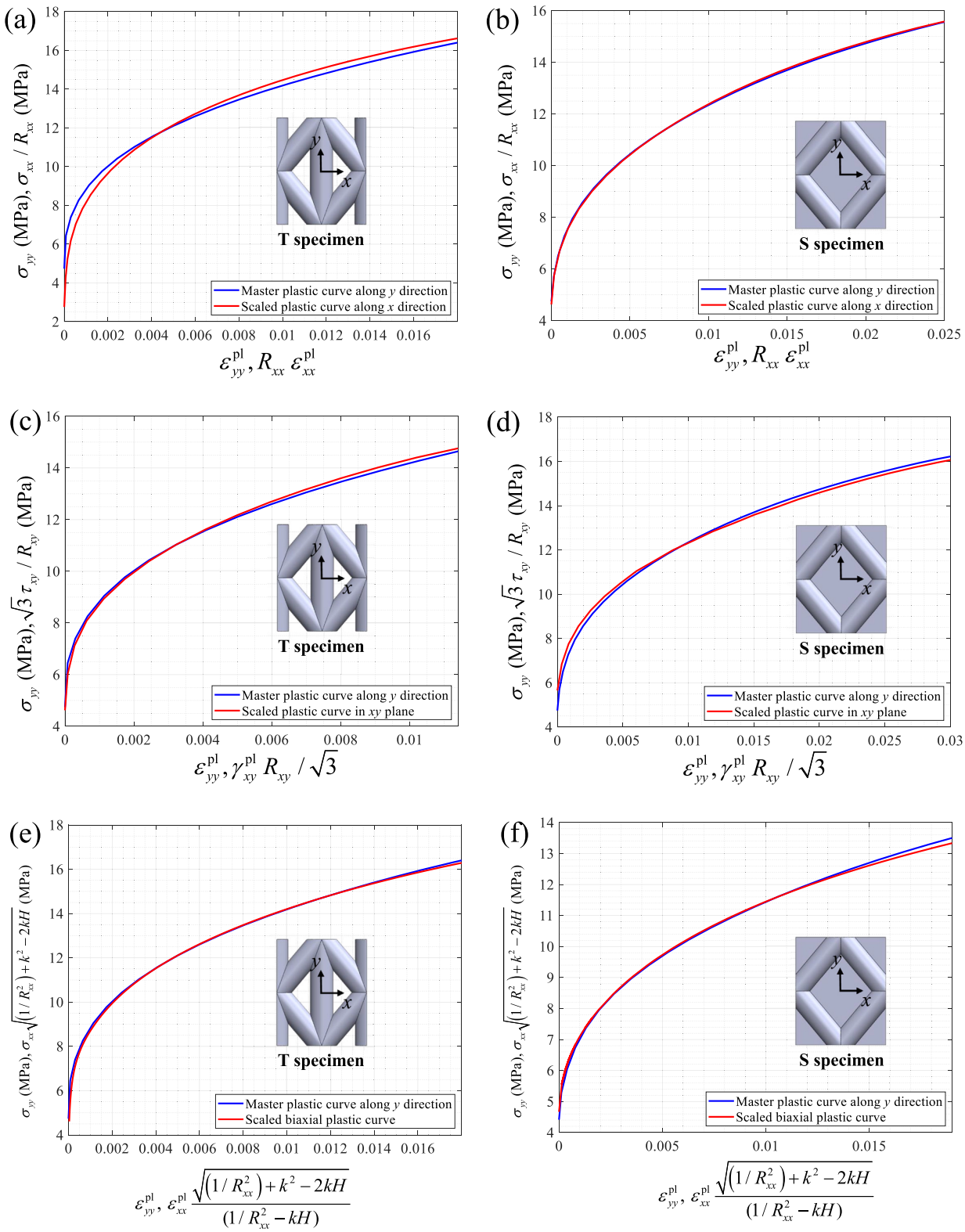


**Fig. 9.** Scaling of the plastic curves of RVEs in the various directions to fit the reference plastic curve along $y$ direction: (a) plastic curve of T specimen after uniaxial loading along $x$ direction, (b) plastic curve of S specimen after uniaxial loading along $x$ direction, (c) plastic curve of T specimen after shear loading in $xy$ plane, (d) plastic curve of S specimen after shear loading in $xy$ plane, (e) plastic curve of T specimen after a biaxial loading in $xy$ plane and (e) plastic curve of S specimen after a biaxial loading in $xy$ plane.

models did not have the aim of reproducing the correct testing conditions for shear or torsional loading cases, while the important thing was that the same boundary conditions were applied to both lattice units and homogenized models. In Figs. 13 and 14 the comparisons between the results of FE simulations of 1/40 of the central layers of T and S specimens and the corresponding homogenized models are presented. In particular, in Figs. 13(a) and 14(a) the results in terms of axial stress $\sigma_{yy}$ and strain $\varepsilon_{yy}$ are shown. Once the FE simulations

**Table 3**
Yielding stresses and Hill model parameters of the homogenized models of RVEs of T and S specimens by varying AR.

| | $\sigma_{0,yy}$ (MPa) | $\sigma_{0,xx}$ (MPa) | $\tau_{0,xy}$ (MPa) | $F$ | $G$ | $H$ | $N$ |
|---|---|---|---|---|---|---|---|
| RVE T specimen (AR = 1.47) | 6.23 | 2.36 | 2.25 | 0.305 | 1.17 | 0.695 | 2.02 |
| RVE T specimen (AR = 1.96) | 4.74 | 1.47 | 2.14 | 0.0680 | 2.58 | 0.932 | 2.34 |
| RVE T specimen (AR = 2.50) | 3.66 | 0.97 | 1.63 | −0.020 | 3.67 | 1.02 | 2.28 |
| RVE T specimen (AR = 2.94) | 2.93 | 0.53 | 1.35 | −0.020 | 3.98 | 1.02 | 2.14 |
| RVE T specimen (AR = 3.50) | 2.35 | 0.48 | 1.13 | 0.001 | 3.99 | 0.999 | 1.98 |
| RVE S specimen (AR = 1.47) | 5.24 | 4.67 | 3.46 | 0.360 | 0.549 | 0.640 | 1.16 |
| RVE S specimen (AR = 1.96) | 4.74 | 4.25 | 3.76 | 0.354 | 0.537 | 0.646 | 1.14 |
| RVE S specimen (AR = 2.50) | 4.42 | 3.98 | 2.87 | 0.369 | 0.534 | 0.631 | 1.14 |
| RVE S specimen (AR = 2.94) | 4.24 | 3.84 | 3.36 | 0.375 | 0.528 | 0.625 | 1.16 |
| RVE S specimen (AR = 3.50) | 4.08 | 3.72 | 3.22 | 0.387 | 0.522 | 0.613 | 1.18 |

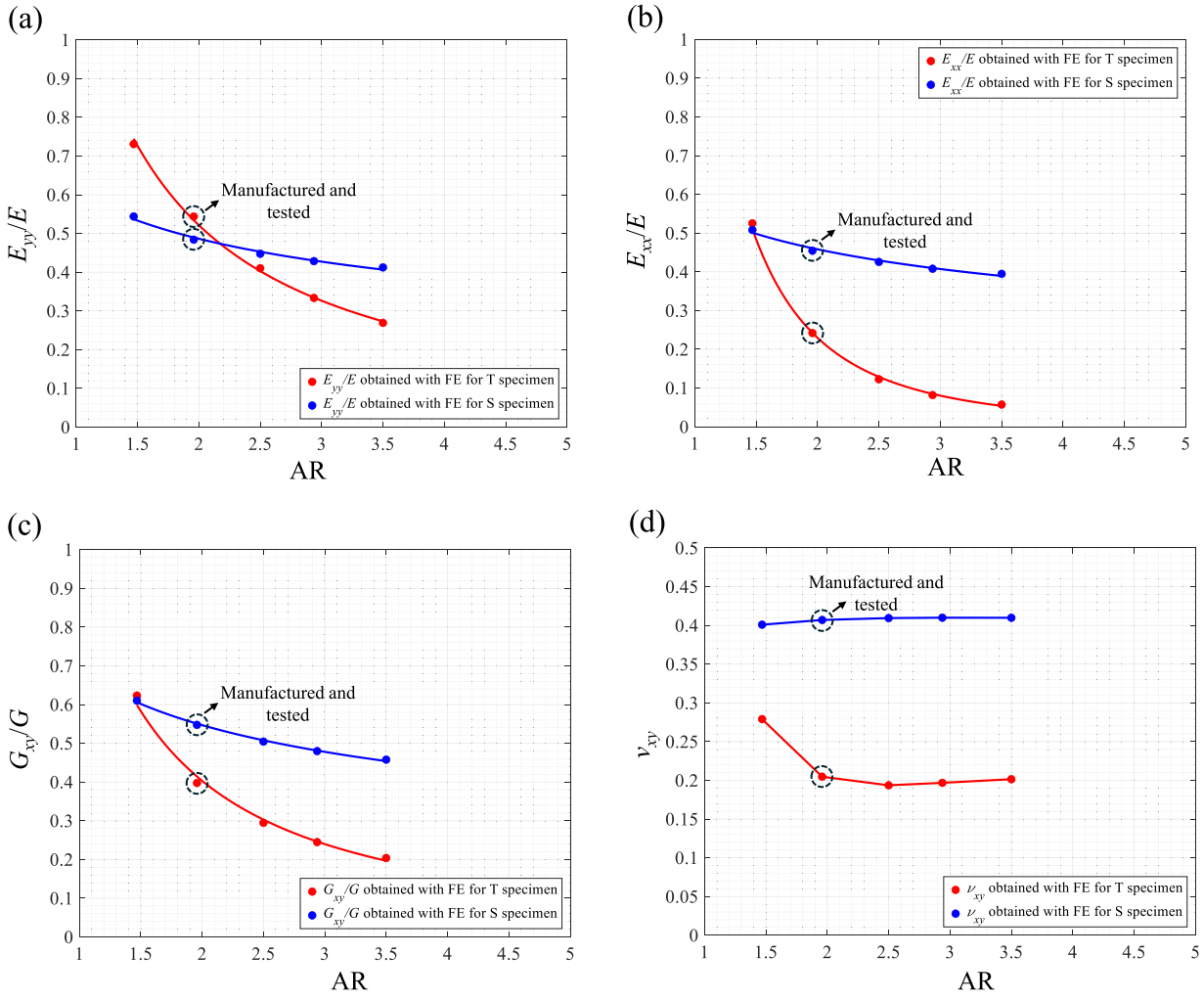


**Fig. 10.** Results of elastic homogenization by varying the aspect ratio: (a) Young modulus $E_{yy}$, (b) Young modulus $E_{xx}$, (c) shear modulus $G_{xy}$ and (d) Poisson ratio $\nu_{xy}$.

were completed, the force $F_y$ and the displacement $u_y$ on the upper surface were extracted. After that, the axial stress was defined as $\sigma_{yy} = 20F_y/(\pi(R_{ext}^2 - R_{int}^2))$ where $R_{ext}$ and $R_{int}$ are the external and internal radii of the cylindrical homogenized models, which inscribe the lattice units. After this, the axial strain was defined as $\varepsilon_{yy} = u_y/a_1$ where $a_1$ is the height of the homogenized models consistently with what shown in Fig. 3. In Figs. 13(b) and 14(b), the comparisons between the results in terms of shear stress $\tau_{\theta y}$ and shear strain $\gamma_{\theta y}$ are shown. Once FE simulations were completed, the axial moment $M_y$ and the circumferential displacement $u_\theta$ were extracted on the upper surface. After that, the shear stress was defined as $\tau_{\theta y} = 20M_y/(\pi(R_{ext}^4 - R_{int}^4)/2R_{ext})$, while the shear strain was defined as $\gamma_{\theta y} = u_\theta/((R_{ext} + R_{int})/2)$, i.e. the rotation of the points at the average thickness of the upper section. The definition of the quantities $\tau_{\theta y}$ and $\gamma_{\theta y}$ was coherent with the cylindrical coordinate systems introduced in Fig. 12.

### 3.2. Tensile tests on lattice specimens

Quasi-static tensile tests on three lattice specimens for each type were conducted using an Instron 8516 universal testing machine as shown in Fig. 15(a) and (b) for T and S specimens, respectively. Fig. 15(c) shows, in mounted configuration, tailored grips that were designed for transferring loads during the tests. The design was inspired by ASTM D638 guidelines; the grips consist of a metal plug and an external clamp secured with three M5 screws to ensure a non-slipping condition and stable grip throughout all phases of tensile testing.

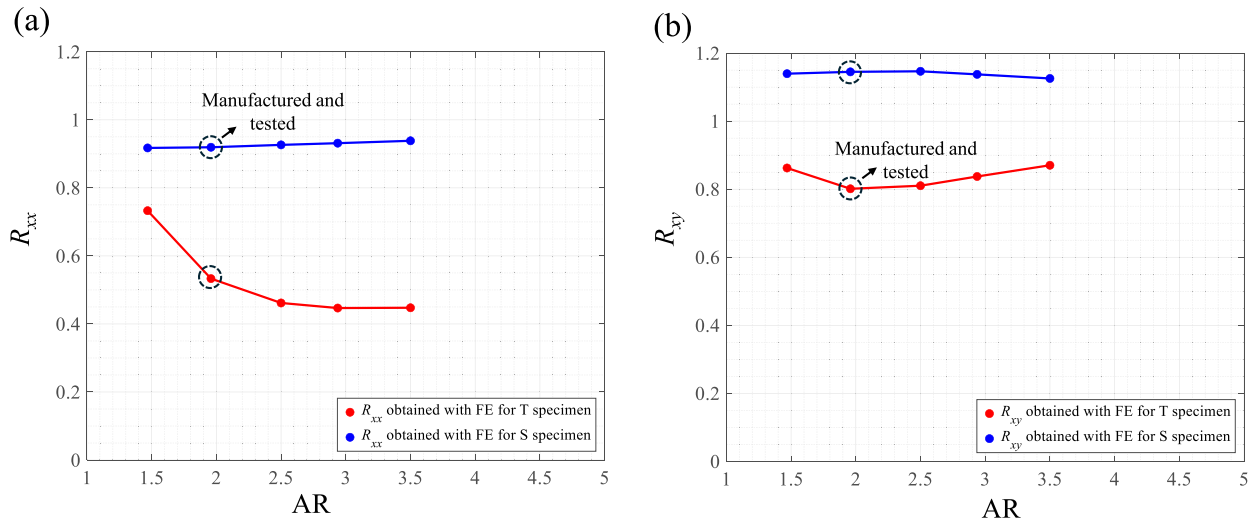


**Fig. 11.** Results of plastic homogenization by varying the aspect ratio: (a) Hill stress ratio $R_{xx}$ and (b) Hill stress ratio $R_{xy}$.

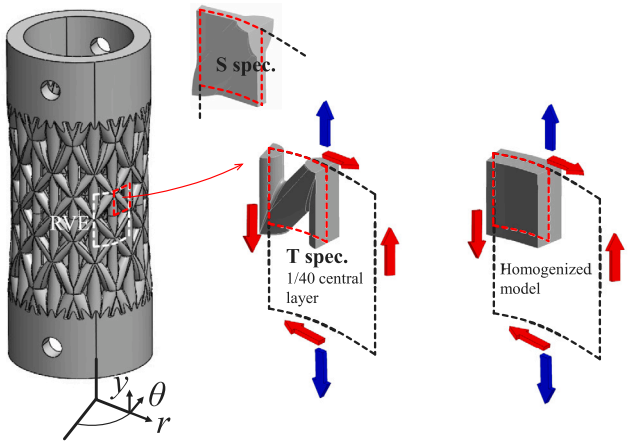


**Fig. 12.** Boundary conditions for FE modelling of tensile loading along $y$ direction and shear loading in $\theta y$ plane for the central layers of T and S specimens and corresponding homogenized models.

The lattice sample was attached to the previously presented specially designed fixture as shown in Fig. 15(a) and (b). To secure the fixtures, both bolts were tightened while pulling the fixture bars apart.

The engineering stress–strain plots for T and S specimens are shown in Fig. 16, and the average experimental curves are also reported with a grey dashed line. These latter were defined until the minimum strain of failure of the tested specimens. The axial stress $\sigma$ was calculated by dividing the force measured by the load cell and the area of the middle section of lattice specimens. All tests were conducted at a loading rate of 0.1 mm/min, with an extensometer attached to the specimen for precise deformation measurement. The extensometer was placed in correspondence of the central layers where the diameters and the helyx angles of the struts were constant as shown in Fig. 15(a) and (b). The axial strain $\varepsilon$ was calculated by dividing the displacement measured by the extensometer $\Delta u_y$ and the initial gauge length $L_0$, which was equal to $L_0 = 10$ mm. All curves exhibit a nearly linear initial response, indicative of elastic deformation, while, as in B specimens, the subsequent part of the curve is characterized by a progressive increment of the nonlinear plastic behaviour.

### 3.3. Experimental validations

After the numerical validations of the elastic–plastic homogenization of central layers of T and S specimens, elastic–plastic FE simulations of homogenized models of entire T and S specimens and of T and S lattice specimens were implemented. The as-designed geometry was used in FE simulations of lattice specimens, and the imposed boundary conditions are shown in Fig. 5(a) and (b) for T and S specimens, respectively. In both cases, symmetries were used, thus 1/40 of the specimen was considered, and nonlinear FE simulations were performed to investigate the elastic–plastic behaviour. The axial displacement, which aims to reproduce tensile testing conditions, was imposed on the upper surfaces of the specimens. On the same faces, all the other degrees of freedom (displacements and rotations) were imposed null according to the constraints provided by the clamping system. The upper surfaces of T and S specimens were taken, in FE simulations, approximately 2 mm below the upper holes of the specimens, which were necessary to block the clamping system during tensile tests. This choice was motivated by the fact that the clamping system was inserted in lattice specimens until approximately 2 mm below the two holes. The boundary conditions of Fig. 5 were also applied in FE simulations of the homogenized models. As shown in Fig. 5, the thicknesses of first and second layers of homogenized models were equal, while they were different between second and third layers. However, this was not a problem in FE simulations given that the same thickness between first and second layers provided the application of a uniform displacement at the interface between the two layers. Once FE simulations were completed, the axial forces $F_y$ were obtained on the upper surfaces of both lattice and homogenized specimens, while the axial displacements $u_y$ were extracted in correspondence of the locations of the strain gauges during the tensile tests, which were located 5 mm higher and lower than the middle surfaces. This latter quantity was employed to calculate the relative displacements of the two extremities of the extensometer, which have an initial distance of $L_0$ as shown in Fig. 17, as $\Delta u_y = 2u_y$. The results of FE simulations together with the average curves obtained from the experimental tests are shown in Fig. 17 for T and S specimens, and the quantity reported on $x$ axis is $\Delta u_y$, while, given that 1/40 of specimens was employed in numerical simulations, the quantity reported on $y$ axis corresponds to the axial force obtained from FE and multiplied by 20.

## 4. Discussion

In this section the discussion of the obtained FE results is provided. In Figs. 13 and 14 the comparisons between the results of

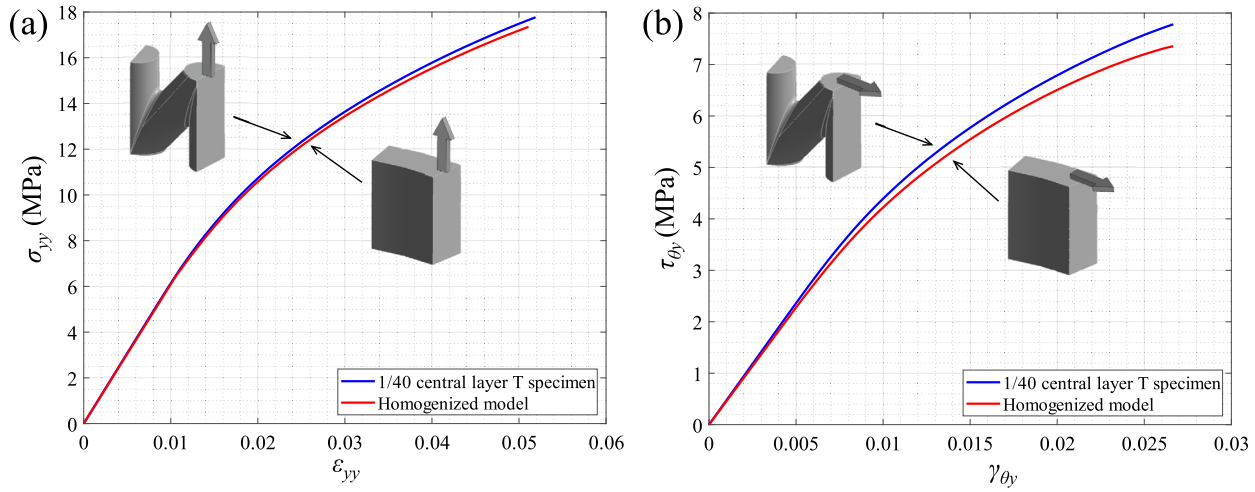


**Fig. 13.** Comparison between the results of FE simulations of 1/40 of central layer and corresponding homogenized model of T specimen: (a) tensile loading along $y$ direction and (b) shear loading in $\theta y$ plane.

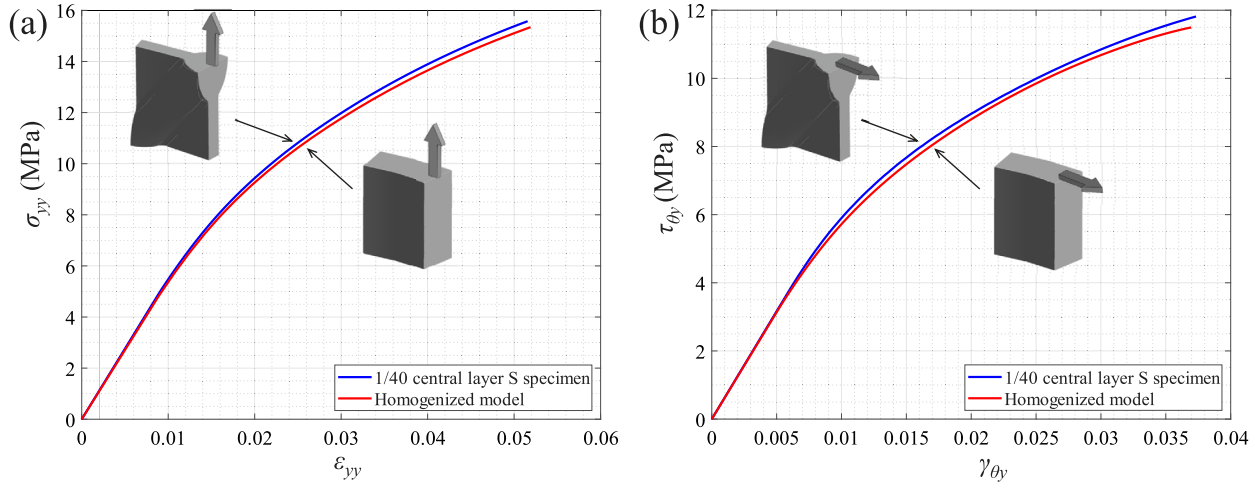


**Fig. 14.** Comparison between the results of FE simulations of 1/40 of central layer and corresponding homogenized model of S specimen: (a) tensile loading along $y$ direction and (b) shear loading in $\theta y$ plane.

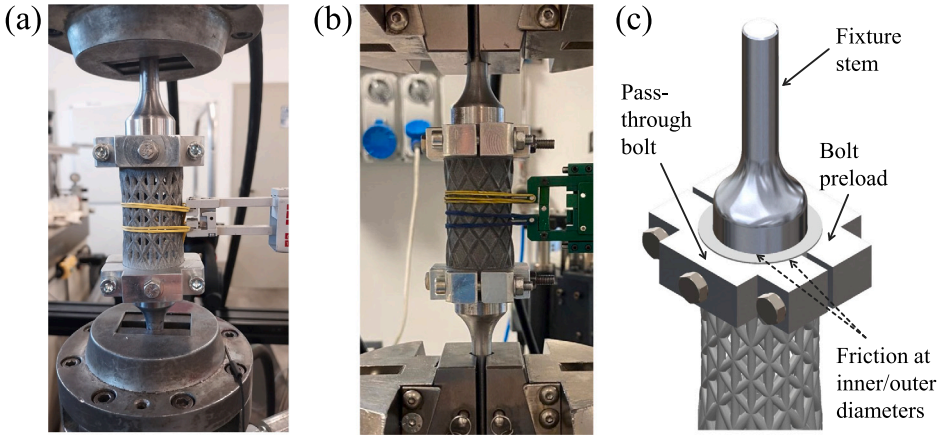


**Fig. 15.** (a) Tensile test on T specimen, (b) tensile test on S specimen and (c) design of the clamping system to perform tensile tests.

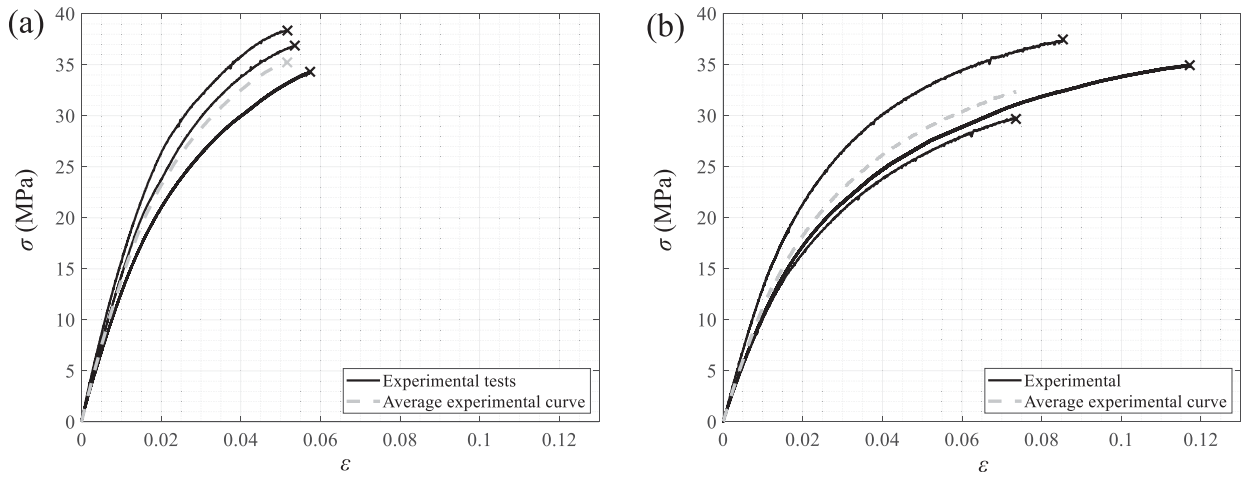


**Fig. 16.** (a) Results of tensile tests on T specimens and (b) results of tensile tests on S specimens.

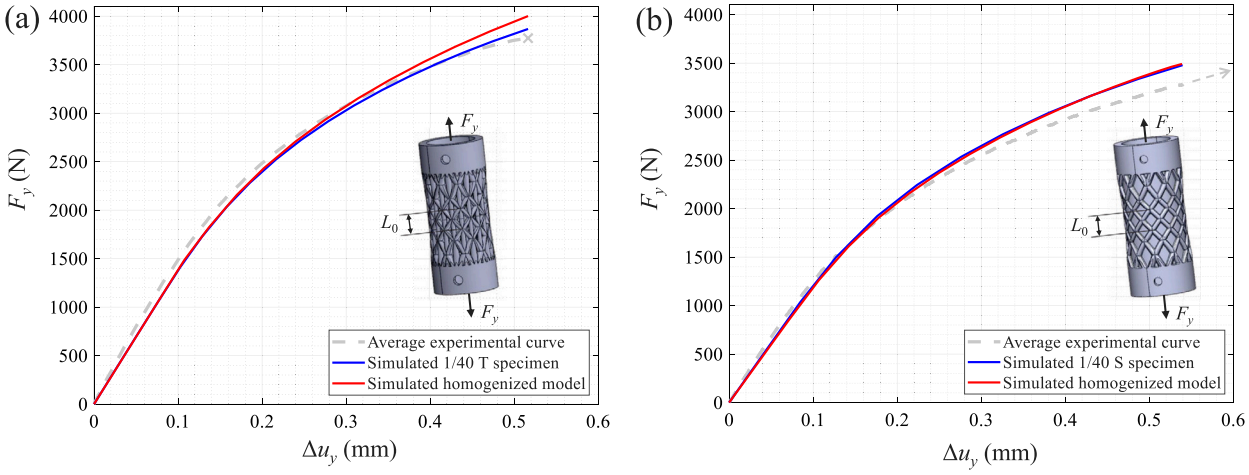


**Fig. 17.** Comparison between experimental results and FE results of simulations along $y$ direction of 1/40 of lattice specimens and corresponding homogenized models: (a) T specimen and (b) S specimen.

FE simulations of 1/40 of the central layers of T and S specimens and the corresponding homogenized models are presented. The results are in good agreement, and the small differences can be explained considering that the mechanical properties of the homogenized models were obtained with FE simulations of planar RVEs, thus neglecting the roundness of the unit cells, and that the fillet radii were not considered in homogenization of RVEs. The discrepancies between the quantities $\tau_{\theta y}$ and $\gamma_{\theta y}$ are higher for T specimen (Fig. 13(b)) than for S specimen (Fig. 14(b)). This can be explained considering that the cross-section of T specimen is an open section for torsional loading cases, thus the use of a planar RVE to calculate shear mechanical properties of the homogenized model inevitably introduce differences with the results of FE simulations of 1/40 of the central layer. In any case, the differences remain lower than 6%. On the other side, very small differences were obtained between the quantities $\tau_{\theta y}$ and $\gamma_{\theta y}$ extracted from FE simulations of 1/40 of the central layer of S specimen and the corresponding homogenized model. In fact, S specimen has a closed cross-section with an important role provided by the cylindrical shell structure, which is considered an optimal shape for torsional loading cases. Finally, the comparisons between the experimental results of tensile tests on lattice specimens and the results of tensile FE simulations of 1/40 of T and S specimens and the corresponding homogenized models are shown in Fig. 17. The ultimate points of the $F_y$-$\Delta u_y$ plots, shown in Fig. 17 and obtained from FE simulations, were imposed by the last point of the lookup table used as input to describe the constitutive bahviour of the bulk material, which was employed to perform FE simulation of 1/40 of lattice specimens and the homogenization process of RVEs. According to this, the last points of Figs. 8 and 9 are also imposed by the last point of the lookup table obtained from B specimen. The last points of the curves obtained from FE simulations coincide with the last point of the average experimental curve for T specimen as shown in Fig. 17(a), while the average curve of S specimen would continue beyond the last point of the grey dashed line as indicated by the grey arrows in Fig. 17(b). For these latter reasons, the plot of the average experimental curve of tensile tests on S specimens was interrupted in correspondence of $\varepsilon \approx 0.055$. The plots of Fig. 17 show that the homogenized models can well replicate the results obtained with FE simulations of 1/40 of T and S specimens and they are also in good agreement with the average curve of experimental results. The differences can be explained considering that as-designed models were employed in FE simulations, thus the unavoidable differences between the as-built and the as-designed geometries were not considered. Despite this, the small differences between the results of FE simulations implemented with the as-designed geometries and the experimental results confirm a small deviation between the as-designed and the as-built geometries.

## 5. Conclusions

In this research B specimens made of PA12 were manufactured with MJF technique, and they underwent tensile tests to characterize the constitutive behaviour of the material. Tensile tests were also performed on two kinds of lattice specimens, named as T and S specimens, with graded strut diameters and variable helyx angle, and that were still produced with MJF and made of PA12. Elastic–plastic homogenization technique was implemented for RVEs of lattice specimens by varying the AR with the objective of identifying the elastic–plastic mechanical properties of the equivalent homogenized models. A simplified approach was also proposed to reproduce, through FE, the different hardening behaviour of RVEs in the various directions. The main findings of the research are emphasized below:

- Tensile tests on B specimens made of PA12 highlighted a first linear elastic zone followed by nonlinear elastic–plastic strains. A similar behaviour was also observed after tensile tests on lattice specimens.
- A loading–unloading test was also performed on a B specimen to investigate the possible hyperelastic behaviour of the material. When the unloading was executed, the axial stress was brought back to zero, the curve did not go back to the origin of stress strain plane and a nonzero hysteresis area was observed. This excluded the use of a hyperelastic material model to characterize the constitutive law of PA12.
- The PBCs were used to perform the homogenization of the identified planar RVEs, and it was obtained that if the lateral faces are of symmetry, the application of PBCs can be simplified.
- The Hill yielding criterion and the Levy-Mises plastic flow rule were combined into a simplified approach to consider the different hardening behaviour of RVEs in the various directions. Firstly, the proposed algorithm consists on identifying a plastic curve of reference. The hardening behaviour of RVEs in the other directions were then modelled by tuning the Hill coefficients that scaled, in an appropriate coordinate system, the curves in the other direction into the reference plastic curve.
- The elastic–plastic homogenization was also implemented by varying the AR of the RVEs with constant strut diameters and helyx angles. After this, power laws were employed to describe the dependence of Young and shear moduli on AR, while piecewise linear functions were used to describe the relationships between Poisson ratio and Hill stress ratios and AR.
- Finally, complete homogenized models, thus including the initial elastic zone and the subsequent elastic–plastic zone, of lattice specimens were obtained, and they were employed in FE simulations showing a good level of agreement with the experimental results and the numerical results obtained from FE simulations of lattice specimens.
- The proposed algorithm for elastic–plastic homogenization and the obtained relationships between the elastic and the plastic properties of homogenized models with AR can be used in structural optimizations in elastic and elastic plastic fields.

## Declaration of competing interest

We wish to confirm that there are no known conflicts of interest associated with this publication and there has been no significant financial support for this work that could have influenced its outcome.

We confirm that the manuscript has been read and approved by all named authors and that there are no other persons who satisfied the criteria for authorship but are not listed. We further confirm that the order of authors listed in the manuscript has been approved by all of us.

We confirm that we have given due consideration to the protection of intellectual property associated with this work and that there are no impediments to publication, including the timing of publication, with respect to intellectual property. In so doing we confirm that we have followed the regulations of our institutions concerning intellectual property.

We understand that the Corresponding Author is the sole contact for the Editorial process (including Editorial Manager and direct communications with the office). He/she is responsible for communicating with the other authors about progress, submissions of revisions and final approval of proofs.

## Funding and acknowledgements

This work was Funded by the European Union - Next Generation EU and supported by the Italian Ministry of University and Research (MUR) in the frame of the programme PRIN 2022 (Avviso DD 104 del 02/02/22) Piano Nazionale di Ripresa e Resilienza (PNRR) – Missione 4 Componente 2, “Dalla ricerca all’impresa” Investimento 1.1, “Fondo per il Programma Nazionale di Ricerca e Progetti di Rilevante Interesse Nazionale (PRIN), project title “Calliope: lattiCe bAsed uLtra Light SensOrized upper limb ProsthEsis”, grant number 2022PRHZM3 - CUP J53D23002380001 (CUP University of Pisa unit I53D23001840006). Link to the website of the project: https://www.calliope-hand.it/

## Appendix A. Supplementary data

Supplementary material related to this article can be found online at https://doi.org/10.1016/j.jmrt.2025.03.137.

## Data availability

Most of the obtained data are presented in the text of the article and in the electronic appendix. The other data will be available on request.

## References

[1] Benedetti M, Du Plessis A, Ritchie RO, Dallago M, Razavi N, Berto F. Architected cellular materials: A review on their mechanical properties towards fatigue-tolerant design and fabrication. Mater Sci Eng: R: Rep 2021;144:100606. http://dx.doi.org/10.1016/j.mser.2021.100606.

[2] Fleck NA, Deshpande VS, Ashby MF. Micro-architectured materials: past, present and future. Proc R Soc A: Math Phys Eng Sci 2010;466(2121):2495–516. http://dx.doi.org/10.1098/rspa.2010.0215.

[3] Nagy D, Zhao D, Benjamin D. Nature-based hybrid computational geometry system for optimizing component structure. Springer Singapore; 2017, p. 167–76.

[4] Chougrani L, Pernot J-P, Véron P, Abed S. Parts internal structure definition using non-uniform patterned lattice optimization for mass reduction in additive manufacturing. Eng Comput 2018;35(1):277–89. http://dx.doi.org/10.1007/s00366-018-0598-2.

[5] Georges H, Mittelstedt C, Becker W. RVE-based grading of truss lattice cores in sandwich panels. Arch Appl Mech 2023;93(8):3189–203. http://dx.doi.org/10.1007/s00419-023-02432-1.

[6] Großmann A, Klyk M, Kohn L, Meyer G, Greiner M, Yang Y, Mittelstedt C. Bioinspired airwings: Design and additive manufacturing of a geometrically graded microscale maple seed. Mater Today Commun 2024;38:108014. http://dx.doi.org/10.1016/j.mtcomm.2023.108014.

[7] Airbus. Pioneering bionic 3D printing - learning from nature. Technical report, Airbus Group; 2016, https://additivemanufacturing.com/2016/01/27/airbus-group-pioneering-bionic-3d-printing-learning-from-nature/.

[8] Osswald PV, Obst P, Mazzei C Gerardo A, Friedrich M, Rietzel D, Witt G. Failure criterion for PA 12 multi-jet fusion additive manufactured parts. Addit Manuf 2021;37:101668. http://dx.doi.org/10.1016/j.addma.2020.101668.

[9] Zhang W, Xu J. Advanced lightweight materials for automobiles: A review. Mater Des 2022;221:110994. http://dx.doi.org/10.1016/j.matdes.2022.110994.

[10] Ricles LM, Coburn JC, Prima MD, Oh SS. Regulating 3D-printed medical products. Sci Transl Med 2018;10(461). http://dx.doi.org/10.1126/scitranslmed.aan6521.

[11] Naghavi SA, Tamaddon M, Garcia-Souto P, Moazen M, Taylor S, Hua J, Liu C. A novel hybrid design and modelling of a customised graded Ti-6Al-4V porous hip implant to reduce stress-shielding: An experimental and numerical analysis. Front Bioeng Biotechnol 2023;11. http://dx.doi.org/10.3389/fbioe.2023.1092361.

[12] Emanuelli L, Jam A, Du Plessis A, Lora C, De Biasi R, Benedetti M, Pellizzari M. Manufacturability of functionally graded porous $\beta$-Ti21S auxetic architected biomaterials produced by laser powder bed fusion: Comparison between 2D and 3D metrological characterization. Int J Bioprinting 2024;9(4):728. http://dx.doi.org/10.18063/ijb.728.
[13] Emanuelli L, De Biasi R, Du Plessis A, Lora C, Jam A, Benedetti M, Pellizzari M. Metrological characterization of porosity graded $\beta$-Ti21S triply periodic minimal surface cellular structure manufactured by laser powder bed fusion. Int J Bioprinting 2024;9(4):729. http://dx.doi.org/10.18063/ijb.729.
[14] DebRoy T, Wei HL, Zuback JS, Mukherjee T, Elmer JW, Milewski JO, Beese AM, Wilson-Heid A, De A, Zhang W. Additive manufacturing of metallic components – Process, structure and properties. Prog Mater Sci 2018;92:112–224. http://dx.doi.org/10.1016/j.pmatsci.2017.10.001.
[15] Ladani L, Sadeghilaridjani M. Review of powder bed fusion additive manufacturing for metals. Metals 2021;11(9):1391. http://dx.doi.org/10.3390/met11091391.
[16] Abd-Elaziem W, Elkatatny S, Abd-Elaziem A-E, Khedr M, Abd E-b Marwa A, Hassan MA, Abu-Okail M, Mohammed M, Järvenpää A, Allam T, Hamada A. On the current research progress of metallic materials fabricated by laser powder bed fusion process: a review. J Mater Res Technol 2022;20:681–707. http://dx.doi.org/10.1016/j.jmrt.2022.07.085.
[17] Avanzini A, Battini D, Pandini S. Static and fatigue behavior in presence of notches for polyamide 12 (PA12) additively manufactured via multi jet fusion™ process. Int J Fatigue 2022;161:106912. http://dx.doi.org/10.1016/j.ijfatigue.2022.106912.
[18] Bazan A, Turek P, Zakrecki A. Influence of antibacterial coating and mechanical and chemical treatment on the surface properties of PA12 parts manufactured with SLS and MJF techniques in the context of medical applications. Mater 2023;16(6):2405. http://dx.doi.org/10.3390/ma16062405.
[19] Koh ZH, Chen K, Du H, Zeng J, Zhou K. Long-term ageing effect on mechanical properties of polyamide 12 printed by multi-jet-fusion. Int J Mech Sci 2023;256:108513. http://dx.doi.org/10.1016/j.ijmecsci.2023.108513.
[20] Puttonen T, Salmi M, Partanen J. Mechanical properties and fracture characterization of additive manufacturing polyamide 12 after accelerated weathering. Polym Test 2021;104:107376. http://dx.doi.org/10.1016/j.polymertesting.2021.107376.
[21] Guo B, Xu Z, Luo X, Bai J. A detailed evaluation of surface, thermal, and flammable properties of polyamide 12/glass beads composites fabricated by multi jet fusion. Virtual Phys Prototyp 2021;16(sup1):S39–52. http://dx.doi.org/10.1080/17452759.2021.1899463.
[22] Chen M, Hou Y, An R, Tey WS, Gao M, Chen J, Zhao L, Zhou K. Investigation of the mechanical properties of polyimide fiber/polyamide 12 composites printed by multi jet fusion. Virtual Phys Prototyp 2023;18(1). http://dx.doi.org/10.1080/17452759.2023.2246032.
[23] Rosso S, Meneghello R, Biasetto L, Grigolato L, Concheri G, Savio G. In-depth comparison of polyamide 12 parts manufactured by multi jet fusion and selective laser sintering. Addit Manuf 2020;36:101713. http://dx.doi.org/10.1016/j.addma.2020.101713.
[24] Mehdipour F, Gebhardt U, Kästner M. Anisotropic and rate-dependent mechanical properties of 3D printed polyamide 12 - A comparison between selective laser sintering and multi jet fusion. Res Mater 2021;11:100213. http://dx.doi.org/10.1016/j.rinma.2021.100213.
[25] Calignano F, Giuffrida F, Galati M. Effect of the build orientation on the mechanical performance of polymeric parts produced by multi jet fusion and selective laser sintering. J Manuf Process 2021;65:271–82. http://dx.doi.org/10.1016/j.jmapro.2021.03.018.
[26] Cai C, Tey WS, Chen J, Zhu W, Liu X, Liu T, Zhao L, Zhou K. Comparative study on 3D printing of polyamide 12 by selective laser sintering and multi jet fusion. J Mater Process Technol 2021;288:116882. http://dx.doi.org/10.1016/j.jmatprotec.2020.116882.
[27] Sillani F, Kleijnen RG, Vetterli M, Schmid M, Wegener K. Selective laser sintering and multi jet fusion: Process-induced modification of the raw materials and analyses of parts performance. Addit Manuf 2019;27:32–41. http://dx.doi.org/10.1016/j.addma.2019.02.004.
[28] Chen K, Koh ZH, Le KQ, Benjamin T How W, Zheng H, Zeng J, Zhou K, Du H. Effects of build positions on the thermal history, crystallization, and mechanical properties of polyamide 12 parts printed by multi jet fusion. Virtual Phys Prototyp 2022;17(3):631–48. http://dx.doi.org/10.1080/17452759.2022.2046478.
[29] O'Connor HJ, Dickson AN, Dowling DP. Evaluation of the mechanical performance of polymer parts fabricated using a production scale multi jet fusion printing process. Addit Manuf 2018;22:381–7. http://dx.doi.org/10.1016/j.addma.2018.05.035.
[30] Marcian LKP, Kajtaz M. Experimental characterisation and finite element modelling of polyamide-12 fabricated via multi jet fusion. Polymers 2022;14(23):5258. http://dx.doi.org/10.3390/polym14235258.
[31] Perez-Barcenilla S, Cearsolo X, Aramburu A, Castano-Alvarez R, Castillo JR, Lopez JG. Applicability of a material constitutive model based on a transversely isotropic behaviour for the prediction of the mechanical performance of multi jet fusion printed polyamide 12 parts. Polymers 2023;16(1):56. http://dx.doi.org/10.3390/polym16010056.
[32] Avanzini A, Tomasoni M, Xu Z, Berto F, Razavi N. Fracture assessment of polyamide 12 (PA12) specimens fabricated via multi jet FusionTM in the presence of geometrical discontinuities. Eng Fract Mech 2024;303:110118. http://dx.doi.org/10.1016/j.engfracmech.2024.110118.
[33] Khorasani M, MacDonald E, Downing D, Ghasemi A, Leary M, Dash J, Sharabian E, Almalki A, Brandt M, Bateman S. Multi Jet Fusion (MJF) of polymeric components: A review of process, properties and opportunities. Addit Manuf 2024;91:104331. http://dx.doi.org/10.1016/j.addma.2024.104331.
[34] Bian Y, Yang F, Zhang S, Chen M, Song Y. Similarities of the mechanical responses of body-centered cubic lattice structures with different constituent materials under compression. JOM 2021;74(4):1774–83. http://dx.doi.org/10.1007/s11837-021-04926-1.
[35] Suquet PM. Homogenization techniques for composite media. Springer Berlin Heidelberg; 1987, p. 193–8.
[36] Salehian A, Inman DJ. Dynamic analysis of a lattice structure by homogenization: Experimental validation. J Sound Vib 2008;316(1–5):180–97. http://dx.doi.org/10.1016/j.jsv.2008.02.031.
[37] Arabnejad S, Pasini D. Mechanical properties of lattice materials via asymptotic homogenization and comparison with alternative homogenization methods. Int J Mech Sci 2013;77:249–62. http://dx.doi.org/10.1016/j.ijmecsci.2013.10.003.
[38] Barchiesi E, Khakalo S. Variational asymptotic homogenization of beam-like square lattice structures. Math Mech Solids 2019;24(10):3295–318. http://dx.doi.org/10.1177/1081286519843155.
[39] Hill R. Elastic properties of reinforced solids: Some theoretical principles. J Mech Phys Solids 1963;11(5):357–72. http://dx.doi.org/10.1016/0022-5096(63)90036-x.
[40] Hashin Z. Analysis of composite materials—A survey. J Appl Mech 1983;50(3):481–505. http://dx.doi.org/10.1115/1.3167081.
[41] Xu S, Shen J, Zhou S, Huang X, Xie YM. Design of lattice structures with controlled anisotropy. Mater Des 2016;93:443–7. http://dx.doi.org/10.1016/j.matdes.2016.01.007.
[42] Mozafari F, Temizer I. Computational homogenization of fatigue in additively manufactured microlattice structures. Comput Mech 2022;71(2):367–84. http://dx.doi.org/10.1007/s00466-022-02243-1.
[43] Somnic J, Jo BW. Status and challenges in homogenization methods for lattice materials. Mater 2022;15(2):605. http://dx.doi.org/10.3390/ma15020605.
[44] Von Hoegen Y, Hellebrand S, Scheunemann L, Schröder J. On the realization of periodic boundary conditions for hexagonal unit cells. Finite Elem Anal Des 2024;229:104067. http://dx.doi.org/10.1016/j.finel.2023.104067.
[45] Wang X, Zhu L, Sun L, Li N. Optimization of graded filleted lattice structures subject to yield and buckling constraints. Mater Des 2021;206:109746. http://dx.doi.org/10.1016/j.matdes.2021.109746.
[46] Xu L, Qian Z. Topology optimization and de-homogenization of graded lattice structures based on asymptotic homogenization. Compos Struct 2021;277:114633. http://dx.doi.org/10.1016/j.compstruct.2021.114633.
[47] Khanoki SA, Pasini D. Multiscale design and multiobjective optimization of orthopedic hip implants with functionally graded cellular material. J Biomech Eng 2012;134(3). http://dx.doi.org/10.1115/1.4006115.
[48] Moussa A, Rahman S, Xu M, Tanzer M, Pasini D. Topology optimization of 3D-printed structurally porous cage for acetabular reinforcement in total hip arthroplasty. J Mech Behav Biomed Mater 2020;105:103705. http://dx.doi.org/10.1016/j.jmbbm.2020.103705.
[49] Ozdemir Z, Tyas A, Goodall R, Askes H. Energy absorption in lattice structures in dynamics: Nonlinear FE simulations. Int J Impact Eng 2017;102:1–15. http://dx.doi.org/10.1016/j.ijimpeng.2016.11.016.
[50] Tallon J, Cyr E, Lloyd A, Mohammadi M. Crush performance of additively manufactured maraging steel microlattice reinforced plates. Eng Fail Anal 2020;108:104231. http://dx.doi.org/10.1016/j.engfailanal.2019.104231.
[51] Sun ZP, Guo YB, Shim VPW. Characterisation and modeling of additively-manufactured polymeric hybrid lattice structures for energy absorption. Int J Mech Sci 2021;191:106101. http://dx.doi.org/10.1016/j.ijmecsci.2020.106101.
[52] Luo Z, Tang Q, Feng Q, Jin M, Ma S, Song J, Han Q. Finite element analysis on mechanical properties of selective laser melting-produced stainless steel 316L lattice structures under impact loading. J Mater Eng Perform 2022;32(1):438–49. http://dx.doi.org/10.1007/s11665-022-07104-9.
[53] Sun ZP, Guo YB, Shim VPW. Static and dynamic crushing of polymeric lattices fabricated by fused deposition modelling and selective laser sintering – an experimental investigation. Int J Impact Eng 2022;160:104059. http://dx.doi.org/10.1016/j.ijimpeng.2021.104059.
[54] Shamim R. Investigation of bending and crush behaviors in polymer lattice structures: Computational approaches and experimental evaluation. J Reinf Plast Compos 2024. http://dx.doi.org/10.1177/07316844241273043.
[55] Gümrük R, Mines RAW, Karadeniz S. Static mechanical behaviours of stainless steel micro-lattice structures under different loading conditions. Mater Sci Eng: A 2013;586:392–406. http://dx.doi.org/10.1016/j.msea.2013.07.070.
[56] Ushijima K, Cantwell WJ, Chen DH. Prediction of the mechanical properties of micro-lattice structures subjected to multi-axial loading. Int J Mech Sci 2013;68:47–55. http://dx.doi.org/10.1016/j.ijmecsci.2012.12.017.
[57] Souza J, Großmann A, Mittelstedt C. Micromechanical analysis of the effective properties of lattice structures in additive manufacturing. Addit Manuf 2018;23:53–69. http://dx.doi.org/10.1016/j.addma.2018.07.007.

[58] Tancogne-Dejean T, Mohr D. Elastically-isotropic truss lattice materials of reduced plastic anisotropy. Int J Solids Struct 2018;138:24–39. http://dx.doi.org/10.1016/j.ijsolstr.2017.12.025.

[59] Mahbod M, Asgari M. Elastic and plastic characterization of a new developed additively manufactured functionally graded porous lattice structure: Analytical and numerical models. Int J Mech Sci 2019;155:248–66. http://dx.doi.org/10.1016/j.ijmecsci.2019.02.041.

[60] Eynbeygui M, Arghavani J, Akbarzadeh AH, Naghdabadi R. Anisotropic elastic–plastic behavior of architected pyramidal lattice materials. Acta Mater 2020;183:118–36. http://dx.doi.org/10.1016/j.actamat.2019.10.038.

[61] Somlo K, Chauhan SS, Niordson CF, Poulios K. Uniaxial tensile behaviour of additively manufactured elastically isotropic truss lattices made of 316L. Int J Solids Struct 2022;246–247:111599. http://dx.doi.org/10.1016/j.ijsolstr.2022.111599.

[62] Hill R. A theory of the yielding and plastic flow of anisotropic metals. Proc R Soc Lond Ser A. Math Phys Sci 1948;193(1033):281–97. http://dx.doi.org/10.1098/rspa.1948.0045.

[63] Pelegatti M, Benasciutti D, De Bona F, Salvati E. Experimental characterization and modelling of cyclic elastoplastic response of an AISI 316L steel lattice structure produced by laser-powder bed fusion. Procedia Struct Integr 2023;47:238–46. http://dx.doi.org/10.1016/j.prostr.2023.07.101.

[64] Chaboche JL. Time-independent constitutive theories for cyclic plasticity. Int J Plast 1986;2(2):149–88. http://dx.doi.org/10.1016/0749-6419(86)90010-0.

[65] Santus C, Romanelli L, Grossi T, Bertini L, Neri P, Le Bone L, Chiesi F, Tognarelli L. Investigation of Chaboche and Bouc–Wen parameters of quenched and tempered steel and comparison of model predictive capabilities. Appl Sci 2023;13(5):2961. http://dx.doi.org/10.3390/app13052961.

[66] Santus C, Grossi T, Romanelli L, Pedranz M, Benedetti M. A computationally fast and accurate procedure for the identification of the Chaboche isotropic-kinematic hardening model parameters based on strain-controlled cycles and asymptotic ratcheting rate. Int J Plast 2023;160:103503. http://dx.doi.org/10.1016/j.ijplas.2022.103503.

[67] Santus C, Romanelli L, Grossi T, Neri P. Determination of Chaboche and Bouc-Wen parameters for quenched and tempered steel. J Theoret Appl Mech 2024;507–19. http://dx.doi.org/10.15632/jtam-pl/188526.

[68] Babamiri BB, Askari H, Hazeli K. Deformation mechanisms and post-yielding behavior of additively manufactured lattice structures. Mater Des 2020;188:108443. http://dx.doi.org/10.1016/j.matdes.2019.108443.

[69] Deshpande VS, Fleck NA. Isotropic constitutive models for metallic foams. J Mech Phys Solids 2000;48(6–7):1253–83. http://dx.doi.org/10.1016/s0022-5096(99)00082-4.

[70] Raghavendra S, Molinari A, Dallago M, Zappini G, Zanini F, Carmignato S, Benedetti M. Uniaxial static mechanical properties of regular, irregular and random additively manufactured cellular materials: Nominal vs. real geometry. Forces Mech 2021;2:100007. http://dx.doi.org/10.1016/j.finmec.2020.100007.

[71] Dallago M, Raghavendra S, Luchin V, Zappini G, Pasini D, Benedetti M. Geometric assessment of lattice materials built via selective laser melting. Mater Today: Proc 2019;7:353–61. http://dx.doi.org/10.1016/j.matpr.2018.11.096.

[72] Murchio S, Dallago M, Rigatti A, Luchin V, Berto F, Maniglio D, Benedetti M. On the effect of the node and building orientation on the fatigue behavior of L-PBF Ti6Al4V lattice structure sub-unital elements. Mater Des Process Commun 2021;3(6). http://dx.doi.org/10.1002/mdp2.258.

[73] Murchio S, Dallago M, Zanini F, Carmignato S, Zappini G, Berto F, Maniglio D, Benedetti M. Additively manufactured Ti–6Al–4V thin struts via laser powder bed fusion: Effect of building orientation on geometrical accuracy and mechanical properties. J Mech Behav Biomed Mater 2021;119:104495. http://dx.doi.org/10.1016/j.jmbbm.2021.104495.

[74] Murchio S, Du Plessis A, Luchin V, Maniglio D, Benedetti M. Influence of mean stress and building orientation on the fatigue properties of sub-unital thin-strut miniaturized Ti6Al4V specimens additively manufactured via laser-powder bed fusion. Int J Fatigue 2024;180:108102. http://dx.doi.org/10.1016/j.ijfatigue.2023.108102.

[75] Gibson Lorna J, Ashby Michael F. Cellular solids: Structure and properties. Cambridge University Press; 1997.